Journal of Solid State Electrochemistry (2022) 26:1809–1838
https://doi.org/10.1007/s10008-022-05206-x

REVIEW PAPER

Recent development in the field of ceramics solid-state electrolytes: I—oxide ceramic solid-state electrolytes

Sumana Kundu[1] · Alexander Kraytsberg[1] · Yair Ein-Eli[1,2]

Received: 18 May 2022 / Revised: 29 May 2022 / Accepted: 29 May 2022 / Published online: 28 June 2022

Abstract

Many elements in the periodic table form ionic compounds; the crystal lattices of such compounds contain cations and anions, which are arranged in the way that these cations and anions form two interpenetrated sub-lattices (cation and anion sub-lattices). Up to now, a number of ionic compounds are known, in which cations or anions are fairly mobile within the corresponding sub-lattice; these compounds are termed as "solid-state electrolytes". Many solid-state electrolytes with such moveable cations and moveable anions are known to date. Following the footsteps of the established Li-ion battery technology, an interest in the Li^+-conducting solid-state electrolytes appears, and all-solid-state lithium battery has started its journey to accompany the reigning counterpart. The valence and ionic radius of ions, the crystal structure, and intrinsic defects of the material are the prime properties of the solid-state electrolytes, which determine the ion mobility in the crystal framework. There are a number of solid-state electrolyte structures that demonstrate high Li^+-mobility and high Li^+ conductivity (Li^+ superconductors) in the range of 10^{-2} to 10^{-3} S/cm at room temperature, which is comparable to the ionic conductivity of 1 M $LiPF_6$ (~ 10^{-2} S/cm), but the conductivity can dwindle highly by up to 5–6 orders of magnitude within the different materials that belonged to the same crystal structure family. Moreover, the surface or interface properties are also crucial factors in tailoring the ionic conductivity of practical polycrystalline solid electrolytes. The interfacial properties and compatibility with electrode materials have a high impact on the performance of electrochemical cells with solid electrolytes. Although the potential window of many solid electrolytes is high enough, there are solid electrolytes which are unstable at low operating potentials while others are not stable towards the cathodes; these features result in the appearance of non-conductive interface layers resulting in a low interfacial charge–transfer kinetics. In this review, we discuss the latest advancements in the field of Li-ion conducting electrolytes from the points of their fundamental properties. The latest achievements in the fields of cell design and improvements of (solid-state electrolytes)/(various anodes) and (solid-state electrolytes)/(various cathodes) compatibilities are considered as well.

Introduction

Crystal lattices of solid ionic compounds contain cations and anions, which form two interpenetrated cation and anion sub-lattices. These compounds demonstrate the feature of ionic conductivity; the phenomenon is that cations and/or anions are somewhat mobile within the corresponding sub-lattice. Such compounds with a reasonably high value of ionic conductivity are commonly termed "solid-state electrolytes" (SSEs). This phenomenon has been known for quite some time; Faraday first discovered this effect examining the conductivity of Ag_2S and PbF_2; during the nineteenth and first half of the twentieth century, a remarkable number of SSEs were discovered [1]. Nevertheless, up to the end of 1960, an operable battery with solid electrolyte was not demonstrated; to the best of our knowledge, specific

This Review is dedicated to Prof. Doron Aurbach's 70th birthday. Doron massively promoted the science and technology associated with portable power sources, water desalination and basic electrochemistry in an immense energy and enthusiasm along his remarkable career. Doron educated and served as an advisor to many generations of Israeli and international scholars. We wish Doron to continue energizing the community, as he did thus far. Cheers!

✉ Yair Ein-Eli
eineli@technion.ac.il

[1] Department of Materials Science and Engineering, Technion - Israel Institute of Technology, 3200003 Haifa, Israel

[2] Grand Technion Energy Program (GTEP), Technion - Israel Institute of Technology, 3200003 Haifa, Israel

designs of such secondary batteries with solid electrolyte (ß-alumina and NASICON-type glassy SSE) were reported only in 1968 [2]. Ag^+-ion cell with $RbAg_4I_5$ electrolyte was the first reversible room-temperature rechargeable cell with solid electrolyte; its description of the cell was first reported in 1969 [3]. First reports on rechargeable Li-ion cells with solid Li^+-conducting electrolyte appear in the beginning of 1990. These were thin film (Li-metal)/TiS_2, (Li-metal)/V_2O_5, and (Li-metal)/$Li_xMn_2O_4$ cells with thin film (~ 1 µm thick) solid electrolytes composed of lithium phosphorus silicates or lithium phosphorus oxynitrides [4]. In some ways, these works may be considered as the starting point of the development of modern rechargeable Li-ion batteries with SSE. A sketch of historical solid electrolyte discovery lineage is presented in Fig. 1 [5, 6], and all the abbreviations are listed in Table 1.

Lithium-ion batteries (LIBs) with liquid electrolyte are composed of cathode and anode separated with electrolyte-permeable (porous) separator and filled with the electrolyte; corresponding active materials are affixed to the cathode and the anode, and the liquid electrolyte is composed of a lithium salt solution in an organic solvent. Usually, both cathode and anode are porous and filled with the electrolyte for providing the Li^+ access on the full thickness of the active material layer of the electrodes. LIBs with solid electrolyte (all-solid-state lithium-ion battery, ASSLIB) are composed of cathode and anode that were separated one from another by the membrane made from SSE. The most common anode material for ASSLIB is metal lithium, and ASSLIB cathodes are composites of active cathode material and SSE; such structure provides Li^+-ions access on the full thickness of the cathode; the thin film versions of ASSLIB (micro-ASSLIB) suggest that both SSE layer and the active cathode material are thin films. Currently, energy storage market is dominated by LIBs with liquid electrolytes because of numerous merits of these LIBs such as high energy density, high cycling efficiency, high cycling, and operational life. LIBs with liquid electrolytes have a number of drawbacks along with these uncontestable merits, though, and these drawbacks are best to be addressed by the substitution of the organic electrolytes with inorganic solid electrolytes.

Table 1 List of abbreviations

ASSB	All-solid-state batteries
LIBs	Li-ion batteries
SSEs	Solid-state electrolytes
SE	Solid electrolytes
NASICON	$Na_{1+x}Zr_2Si_xP_{3-x}O_{12}$,$(0<x<3)$, sodium superionic conductor
LISICON	Lithium superionic conductor, γ-Li_3PO_4-type oxides
LATP	$Li_{1+x}Al_xTi_{2-x}(PO_4)_3$
LAGP	$Li_{1+x}Al_xGe_{2-x}(PO_4)_3$
LLZO	$Li_7La_3Zr_2O_{12}$
SEI	Solid electrolyte interface
CTE	Coefficients of thermal expansion
ASSLIB	All-solid-state lithium-ion battery
LTP	$LiTi_2(PO_4)_3$
LGP	$LiGe_2(PO_4)_3$
LFP	$LiFePO_4$
BN	Boron nitride
LZP	$LiZr_2(PO_4)_3$
LMO	$LiMn_2O_4$
LCO	$LiCoO_2$
NCM	$LiNi_{1/3}Co_{1/3}Mn_{1/3}O_2$
SPS	Spark plasma sintering
LLZO	$Li_7La_3Zr_2O_{12}$
GB	Grain boundaries
LLTO	$Li_{3x}La_{2/3-x}TiO_3$
CV	Cyclic voltammetry
LGVO	$Li_{3.5}Ge_{0.5}V_{0.5}O_4$
LiPON	$Li_xPO_yN_z$
DFT	Density functional theory
RFMS	Radio frequency magnetron sputtering
ALD	Atomic layer deposition
PVP	Physical vapour deposition
CVD	Chemical vapour deposition
PLD	Pulsed laser deposition

- Most of organic electrolytes are flammable, whereas most of solid electrolytes are safe in this regard; the implementation of solid electrolytes reduces the number of combustible materials making the energy storage system safer.

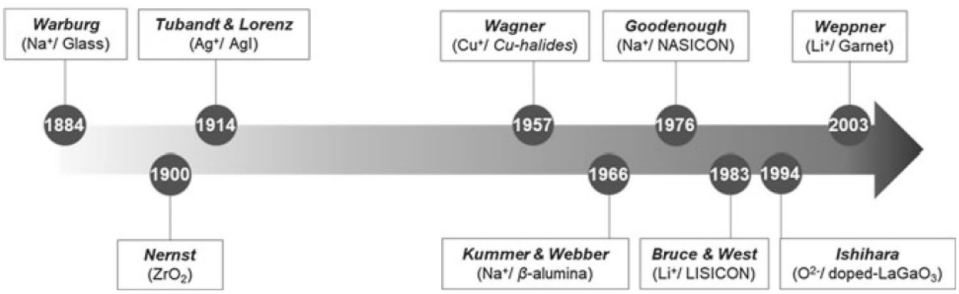

Fig. 1 A historical outline of the development of solid-state electrolytes (reproduced with permission from [5])

- Many SSEs have voltage stability windows much wider than any liquid electrolyte allowing implementation of high-voltage cathode active materials; also, the SSE layer may be prepared as thin as 1 μm, in contrast with standard 25 mm in case of separator for Li-ion cell with liquid electrolyte. These facts make possible further increase of the energy density of Li-ion cell on switching from liquid to solid electrolytes.
- Li-ion batteries with liquid electrolytes and Li-metal anodes are plagued with formation of Li-dendrites, whereas solid electrolytes may eliminate or considerably hinder dendrite growth; the implementation of Li-metal anodes substantially increases the specific energy of the battery.
- On one hand, operation temperature window of a liquid electrolyte is limited by the liquid phase stability temperature, and a battery may be destroyed by electrolyte boiling; on the other hand, frozen electrolytes lose their conductivity. Temperature operation windows of solid electrolytes are substantially wider than the temperature operation windows of liquid electrolytes; SSEs can function at lower temperatures than freezing points of most liquid electrolytes and at higher temperatures than boiling points of most liquid organic electrolytes.
- There are also some integration advantages of ASSLIB: the cells with SSE may easily be stacked in a bipolar arrangement forming a high-voltage body, thus providing simplified system architecture.

ASSLIBs, due to the outlined advantages, have attracted a lot of attention in recent decades [7–14]. While Li^+-conductive SSE can be divided into the following categories: inorganic crystalline and amorphous (glass-type) materials, organic polymer materials, and composite electrolytes (which are a mix of inorganic particles and (organic or inorganic) solid electrolyte matrix), this review is solely focused on the current development in the field of inorganic oxide Li^+-conductive SSEs and ASSLIB with such SSEs.

From ASSLIB design requirements point of view, SSE should be prepared in compact sheet (thin pellet, membrane) form (Fig. 2). Regarding inorganic SSE, while monocrystalline SSEs were reported [15, 16], most of the reported SSE materials had a polycrystalline or amorphous (glass-type) structure. Although preparation of amorphous and polycrystalline thin SSE films was reported [17], the most common methods of SSE preparation are (i) a melt-quenching (glass–ceramic) synthesis, (ii) a solid-state synthesis, and (iii) wet-chemistry synthesis followed by the prepared SSE powder sintering [18–20]. Whereas monocrystalline and film-like SSEs form compact membranes in a natural way, the latter three preparation processes first result in powdered SSE material:

(i) According to the melt-quenching (glass–ceramic) process, precursor ingredients are mixed and then the mix is melted in a crucible followed by pouring the melt into moving rolls of rolling machine or onto a massive metal plate; thus, compact glass SSE sheets are formed; these glass ceramics subsequently undergo crystallizing at a moderate temperature [21, 22]. The morphology of such sheets often features the presence of micro-voids, though. The

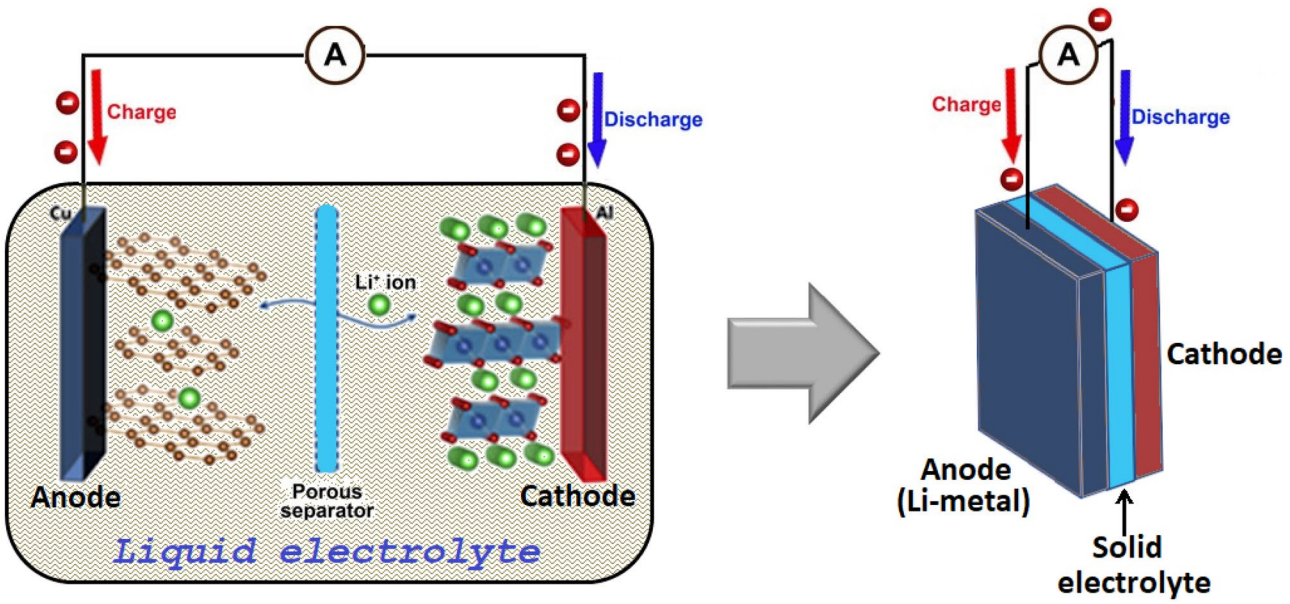

Fig. 2 Li-ion cell with liquid and solid electrolytes. Acquired and modified from [5]

micro-voids result in the reduced density of the SSE sheets, compromises the SSE sheets ionic conductivity, and induces dendrite growth; also, SSE sheet cracks may be induced because of high mechanical stress that originated from a large temperature gradient between the outside and inside SSE sheet surfaces that appeared in the course of quenching [23]. The issue is commonly handled by complementing of the melt-quenching with ceramic processing. For this end, the melt-quenched glass or glass/crystalline SSE bodies are grinded, the powder is pressed into green pellets, and the pellets are sintered [24, 25]. The sintering is conducting at temperatures 50–80% of the melting temperature; the compacting of the powder takes place because of atomic inter-diffusion between the powder particles [26].

(ii) Regarding solid-state SSE syntheses, these processes are in some respects similar to the sintering of melt-quenched SSE powder; the difference is that powdered precursor ingredient mixes do not go through melting but are directly pressed into green pellets and undergo heat treatment at temperatures below melting point, so that atomic inter-diffusion between the powder particles comes along with chemical reactions, and SSE material appears.

(iii) The essence of the wet chemistry preparation is that SSEs appear as the result of liquid-state reactions; for this end, the suited set of initial compounds is dissolved in a proper solvent. The initiated liquid-state interactions of the compounds result in precipitation of the corresponding SSE precursor; this is after the sediment undergoes a thermotreatment. At this stage, the prepared SSE material is in a powder form; the compunction is achieved by ceramic processing (sintering) [27–29].

Thus, up to now, most of the results in the field of inorganic SSE were based on polycrystalline ceramic-type SSE material studies, and most of the experimental ASSLIBs with inorganic SSE were prepared using polycrystalline or glass-type ceramic SSE.

The common requirements for ceramic SSE material to be used for ASSLIB are:

- High Li^+ conductivity: It is noteworthy that conductivity of polycrystalline SSE is composed of two consecutively connected constituents, i.e. in-grain (bulk) conductivity and interface (grain-to-grain contacts) conductivity.
- Low SSE electronic conductivity: This parameter governs the battery self-discharge and the energy efficiency of battery cycling.
- Li^+-transference number should be close to 100%; this is the case for most current ceramic SSE, though.
- Chemical and electrochemical stabilities at the cathode/SSE interface.

Regarding chemical stability at the SSE/(active cathode material) interface, it should be considered not only in the battery operational temperature interval, but also considering the ASSLIB preparation technology temperature requirements. There is an apparent necessity of having the SSE/(cathode active material composite) with intimate contacts between SSE grains and cathode material grains; Fig. 3 schematically presents typical morphology of such SSE/(cathode active material) composite body. The point is, though, that most of the active cathode materials are powdered oxides, and that generally, oxide-based compounds are characterized by their firmness and fragility, so sintering is a common way to prepare the SSE/(cathode active material) composite structures with the required morphology in the case of oxide-based SSEs.

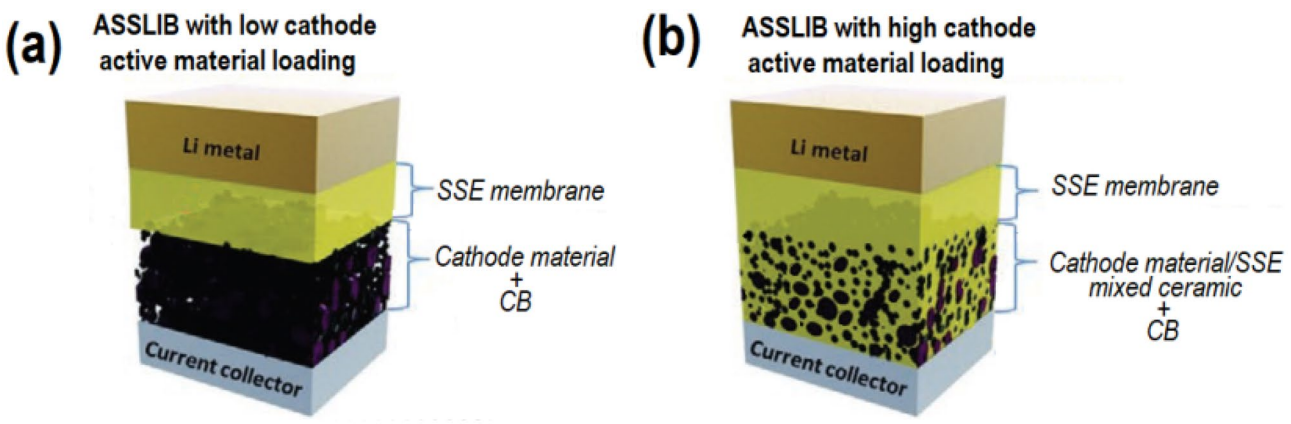

Fig. 3 (**a**) ASSLIB with compact cathode, low active cathode material loading per the electrode area unit; (**b**) ASSLIB with composite cathode, high active cathode material loading per the electrode area unit (modified figure reproduced with permission from [30])

As a result, green pellets of SSE/(cathode active material) mix undergo heating in the course of sintering; on one hand, the heating temperature should be high enough for providing the pellet sintering, and on the other hand, SSE and cathode active material should not enter into chemical reactions at sintering temperatures. The best is if such reactions are thermodynamically disadvantageous; at least, the reaction rates should be significantly lower than the sintering rate.

- Mechanical stability at the cathode/SSE interface.
- The serious source of Li-ion transport failure is the mechanical degradation of the SSE/(cathode material) interface. The delamination of the SSE/(cathode material) contacts with cycling originates from volume changes of cathode material with Li^+ intercalation/deintercalation [31]. These changes result in "breathing" of linear dimensions of the cathode side of the interface and in appearance of periodical tensile and contraction stresses; these stresses finally result in SSE/(cathode material) contacts delamination, build-up of the Li^+-ion transport resistance, and the ASSLIB cycling fade. Overall, the delamination rate and degree depend on cathode expansion coefficient (the expansion of 1 mol of cathode per intercalation of 1 mol of Li^+), the elasticity and hardness of SSE and cathode material (typical values of these parameters certify that commonly oxide SSEs are fragile materials [32]), and [SSE]/[cathode material] interface adhesion [33].
- Chemical and electrochemical stabilities at the lithium/SSE interface are a very desirable property since the most advantageous ASSLIB designs suggest the implementation of Li-metal anode.
- A wide electrochemical stability window in order to benefit from the high-voltage cathode material implementation.
- Good thermal stability: The requirement is mostly related to the SSE interaction with metal Li on heating evolved in the case of dendrite formation on ASSLIB charging.
- The morphology of the ceramic SSE material should inhibit dendrite formation.
- The adequate mechanical strength is also an advantage; besides, the feature is very important for ASSLIB manufacturing.

Brief introduction into Li^+ conduction mechanisms in ceramic SSEs

The basic assumption regarding inorganic crystalline Li^+–SSE bulk ionic conductivity phenomenon is that vacancies, in lattice and interstitials in cationic sub-lattice, are treated as being charged moveable species [34, 35]. Three types of cation migration are commonly taken into consideration; these types are listed below and also are being illustrated in Fig. 4.

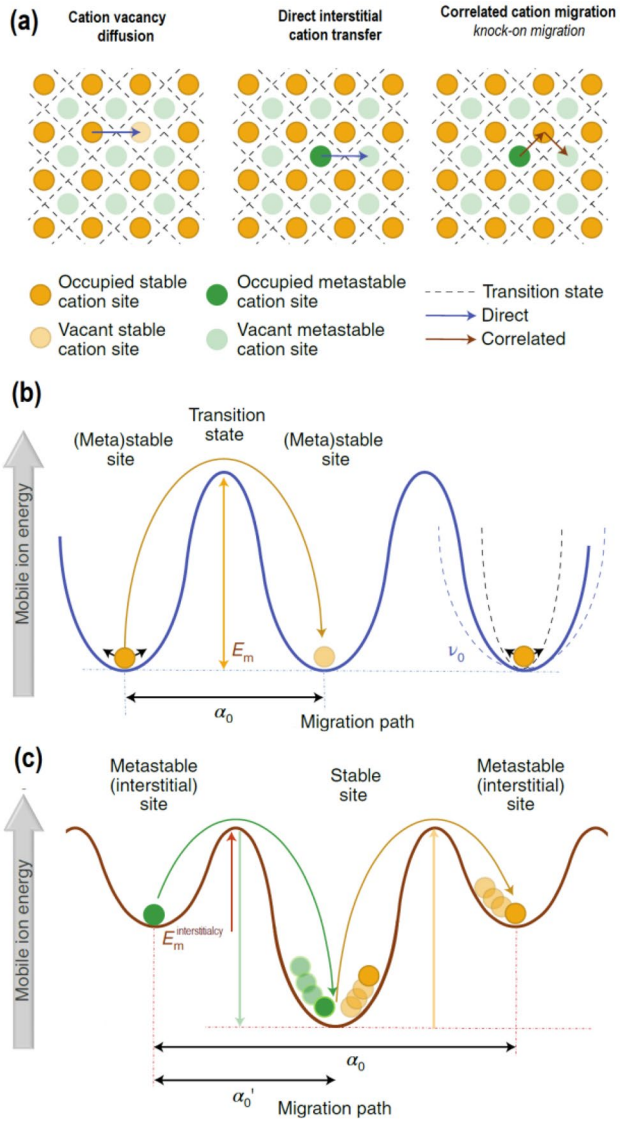

Fig. 4 Cation migration mechanisms and associated energy profiles. (**a**) The arrows indicate three typical migration mechanisms: vacancy, direct interstitial and correlated (interstitialcy) involving a single or multiple sites (blue and red, respectively). Circles represent cations in stable (green) and metastable (orange) sites of a model crystal lattice. Dotted lines represent the transition state for cation hopping as imposed by the anionic framework (not shown explicitly). (**b**, **c**) The energy profiles associated with cation migration via direct vacancy or interstitial hopping (**b**) and correlated hopping (**c**) are shown with their associated hopping energies, E_m, hopping distances α_0 and hopping frequencies, ν_0 (reproduced with permission from [35])

It is noteworthy that only a fraction of cations in a lattice has an ability to move having vacant stable or meta-stable lattice nodes within reach. Figure 4(a–c) illustrate the processes (i), (ii), and (iii) that make up the ionic drift phenomenon in SSE.

(i) Cation vacancy diffusion: Physically, this mechanism corresponds to a cation hopping from its initial position into the adjacent vacant lattice site.

(ii) Direct interstitial cation transfer between partially occupied interstitial (meta-equilibrium) positions.
(iii) Correlated cation migration (knock-on migration); according to this mechanism, the interstitial ion migrates toward adjacent lattice node displacing the occupying ion into the next site.

Amorphous (glass) inorganic SSEs potentially present some substantial advantages over polycrystalline ceramic SSE in respect of flexibility, uniformity, and dense morphology; these materials do not demonstrate grain boundary resistance and grain boundary related anisotropy of Li^+ mobility. These attractive features stimulated the extensive attempts to understand the mechanism of cationic conductivity in amorphous SSEs. While a wealth of experimental data on the amorphous Li^+–SSEs are reported up to now, a detailed mechanism of ion conductivity in amorphous SSE is still not well understood, and no universal theory of glassy SSE is developed. In this context, the principal challenges are that such materials not only have no long-range crystalline order and thus regular symmetrical long-range ion migration pathways, but also do not have regular symmetric short-range coordination order. The latter circumstance makes it difficult to develop a theory of the elemental cation hopping. Despite of a lack of a universal theory for describing Li^+-ion mobility in various types of amorphous SSEs, several hypotheses have been offered for explaining the phenomenon [36–38].

The latest development in the fields of inorganic oxide ceramic Li-ion SSE

Li^+-conducting oxide SSEs may be classified into the following six groups on the basis of their atomic structure, and we will heavily discuss each of the listed materials below:

- NASICON-type.
- Garnet-type.
- Perovskite-type.
- Anti-perovskite-type.
- LISICON-type.
- Amorphous oxides.

NASICON-type Li-ion SSE

Conductivity of the Li.$^+$-NASICON-ceramics In 1976, Goodenough first named a 3D network of superionic Na ion conductor, with a formula $NaMe_2(PO_4)_3$ (here Me stands for four valence metals, [Me^{+4}], like Ge, Ti, Sn, Hf, and Zr), partially substituted P by Si, as NASICON ($Na_{1+x}Zr_2Si_xP_{3-x}O_{12}$, $0<x<3$); these types of materials were studied earlier in the 1960s [39, 40]. Following this report, Li^+ versions of NASICON-type compounds attracted a substantial attention as promising SSE for ASSLIB; numerous NASICON-type compounds $LiMe_2(PO_4)_3$ were prepared and studied for Li^+–SSE [41–47]. Whereas most of these Li^+-NASICON compounds had a rhombohedral symmetry, compounds with triclinic distortion also are found. The framework of these materials composed of $Me_2(PO_4)_3$ units; these units are assembled so that two MeO_6 octahedra have common oxygen atoms with three PO_4 tetrahedra forming a 3D scaffold of the material. Inside this scaffold, Li^+-ions are usually located in M1 sites. M1 sites are positioned between two MeO_6 octahedra being surrounded by six oxygen atoms, and each M1 site is surrounded by six empty M2 sites; the M2 site is "a double site" composing of two M3 and M'3 sites with the same energy. The process of Li^+ conductivity composes of cooperative transport of Li^+-ions from the M1 site to the nearest M1 site through the midway M2 site. The energy barrier between M1 and M2 hinders Li^+ transition and presents a kind of "bottleneck" obstructing the Li^+ conductivity [48, 49]. The need of penetrating through this barrier results in a very low cation conductivity of $LiMe_2(PO_4)_3$ compounds. For instance, NASICONs $LiTi_2(PO_4)_3$ (LTP) and $LiGe_2(PO_4)_3$ (LGP) with rhombohedral symmetry lattices are providing the most favourable frameworks for Li-ion migration, but the reported conductivity of $LiTi_2(PO_4)_3$ is 4.4×10^{-8} S/cm, and the reported conductivity of $LiGe_2(PO_4)_3$ is 5.9×10^{-9} S/cm [50].

The conductivity of Li^+-NASICONs may be substantially enhanced by aliovalent substitution. $Li_{1+x}Me_{2-x}M_x(PO_4)_3$ preserves NASICON structure on partial metal Me substitution for a three-valence metal M (here M stands for M^{+3} metals like Al, Y, etc.) in $LiMe_2(PO_4)_3$ compound, while the material structure turns to be more dense, and Li^+ concentration increases. The additional Li^+ partially populates sites M3 and M'3, which in turn decrease M1 site population; this circumstance assists Li^+ hopping between adjacent partially populated Li^+ sites facilitating long-range Li^+ migration along conductive pathways through the SSE [51–55]. This approach is now dominated in NASICON SSE development, and a number of $Li_{1+x}Al_xTi_{2-x}(PO_4)_3$ (LATPs) and $Li_{1+x}Al_xGe_{2-x}(PO_4)_3$ (LAGPs) NASICONs with improved conductivity were reported [56]. Up to now, 5.1×10^{-3} S/cm for total conductivity of $Li_{1.2}Al_{0.2}Ti_{1.8}(PO_4)_3$ ceramic [57] was reported as the highest conductivities of NASICON SSE ceramics; regarding in-grain conductivity, such values at 2.77×10^{-4} S/cm (in-grain conductivity of $Li_{1.8}Al_{0.2}Zr_{1.8}(PO_4)_3$ ceramic [54]), 7.76×10^{-4} S/cm (in-grain conductivity of $Li_{1.5}Al_{0.5}Ge_{1.5}(PO_4)_3$ ceramic [58]), 5.826×10^{-3} S/cm (in-grain conductivity of $Li_{1.5}Al_{0.33}Sc_{0.17}Ge_{1.5}(PO_4)_3$ ceramic [59]), and 5.63×10^{-3} S/cm (in-grain conductivity of $Li_{1.4}Al_{0.4}Ti_{1.6}(PO_4)_3$ ceramic [60]) were reported.

The total conductivity of the polycrystalline ceramic SSE body depends on the in-grain and inter-grain (contact) resistances to the Li^+ transport connected in series; in most cases, the inter-grain resistance is significantly higher than

the in-grain resistance [51, 61, 62], so substantial efforts have been invested in improving the inter-grain lithium-ion mobility.

It is currently thought that a low inter-grain conductivity is related to the following factors:

- The presence of voids and cracks at the grain interface is compromising Li^+ inter-grain mobility; the feature goes hand in hand with low ceramic SSE density compared with the theoretical X-ray density of the material.
- The presence of alien phases at grain interfaces; the phases appear in the course of SSE ceramic sintering, and these phases may suppress Li^+ mobility.
- The grain lattice distortions at the grain boundaries. The corresponding lattice mismatch at grain interfaces results in formation of charged double-layer structure, and such interface structure constitutes a substantial impediment to Li^+ mobility even in the absence of boundary-related alien phases or such morphological barriers as submicron cracks and voids.

(i) The influence of the grain interfaces morphology on the inter-grain conductivity: The influence of the grain interface morphology on the inter-grain conductivity and the ways of the control of the interface morphology are well reported. Various methods of the SSE ceramic compactness control were employed by different authors, and it was demonstrated that the increase of the density of SSE ceramic usually goes hand-in-hand with enhancement of inter-grain conductivity.

✔ Preparation of LATP ceramic with enhanced density by intermixing precursor powders with bimodal particle size distribution [63] and by applying a particular complex sintering procedures [64, 65] was reported; it was demonstrated that the increase of the ceramic density is accompanied with suppressing of grain border defect concentration and inter-grain voids and the enhancement of inter-grain conductivity.

✔ The other avenue of the grain interface modification on behalf of inter-grain conductivity enhancement is the employment of sintering aids. In this way, grain interfaces of $Li_{1.3}Al_{0.3}Ti_{1.7}(PO_4)_3$ were modified by the addition of $SnO–P_2O_5–MgO$ glass (SPM, 0.7 wt%) [66], B_2O_3 and Bi_2O_3 [67, 68], $Li_{2.9}B_{0.9}S_{0.1}O_{3.1}$ [69], and Li_2WO_4 (7 w. %) [70]. The glass-forming sintering aids increase the ceramic densities favouring grain growth and patching up the interface voids and cracks; it was demonstrated that the sintering aids are securing the grain fitting, thus increasing the inter-grain SSE conductivity; the effect is illustrated in Fig. 5 [71].

(ii) The presence of alien phases at grain interfaces: LATP/LAGP SSE conductivity is plagued by the presence of secondary phases at the grain interface; most of these phases, which form in the course of sintering, are poorly Li^+-conductive. The most common phases are berlinite $AlPO_4$ and also a complementary $LiTiOPO_4$ phase [51, 72, 73]. It was demonstrated that the excess of phosphorus and elevated sintering temperatures are favourable for berlinite formation [74], whereas the phosphorus deficiency favours formation of $LiTiOPO_4$ [75]. Regarding the secondary phases, their action is more complicated than a mere formation of continuous low-conducting shells around SSE grains [51]. It was reported that berlinite forms nano-sized particles, and these particles are concentrating at the SSE grain boundaries; Li^+-ions are adsorbing onto these particles during the ion inter-grain passage. This process results in the appearance of the positive space charge at the grain interfaces:

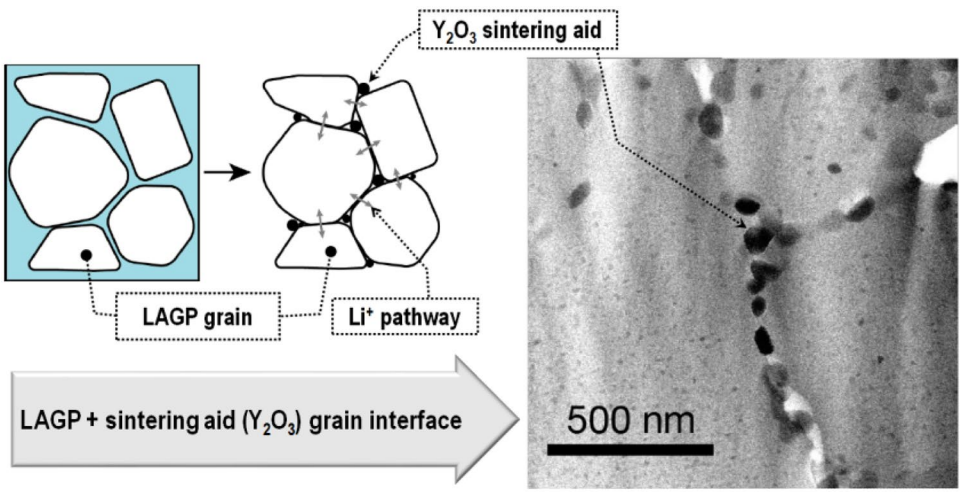

Fig. 5 Grain border fitting improvement by sintering aid, LAGP ceramic, and Y_2O_3 sintering aid (modified figure reproduced with permission from [71])

$AlPO_4 + Li^+ \leftrightarrow [AlPO_4]^{Li^+}_{Li^+}$

The space charge limits the transport of Li^+ through the grain interfaces, and Li^+ inter-grain passage hindrance intensifies as the interface berlinite particles become more numerous and/or larger [76].

These findings highlight the role of interface insulating phases in inter-grain conductivity of NASICON-type SSE and substantiate the efforts for diminishing the formation of the insulating secondary phases. The common approach is the employment of sintering aids; the presence of sintering aids markedly lowers the SSE ceramic sintering temperatures limiting the formation of insulating berlinite, substituting it for Li^+-ion conductive phases.

✔ LATP fluorination reduces the formation of secondary phases (viz. $AlPO_4$ and $LiTiOPO_4$) on the SSE sintering improving the SSE inter-grain and total conductivity; total conductivity of the $Li_{3.6}Al_{0.8}Ti_{4.0}P_{7.6}O_{29.75}F_{0.5}$ was reported to be 3.85×10^{-5} S/cm (at room temperature) [77].

✔ The sintering of LATP ceramic with Li_4SiO_4 and LiF sintering aids results in the appearances of Li^+-conducting interface phases (viz. $LiTiPO_5$, $LiAlP_2O_7$), thus improving the inter-grain conductivity [78, 79].

✔ The sintering of $Li_{1.3}Al_{0.3}Ti_{1.7}(PO_4)_3$ ceramic with $0.75 \cdot Li_2O \times 0.25 \cdot B_2O_3$ [80] and $LiBO_2$ [81] as sintering aids results in decomposition of inter-grain berlinite and other insulating aluminophosphate phases and formation of some lithium conducting phosphates instead. The process is accompanied with the increase of inter-grain conductivity of the SSE ceramic.

(iii) The impact of grain lattice distortions at the grain boundaries on inter-grain conductivities: SSE grain lattices undergo misalignment and accompanied distortion at the interfaces; Fig. 6a and b demonstrate this feature of SSE ceramics; this Å-scale interface phenomenon constitutes a substantial impediment to Li^+ inter-grain transport [83–85]. Naturally, the border between two misaligned grains is a layer with some thickness; it was demonstrated that the conductivity of such transition layer strongly depends on the layer thickness; the interface with sharp transition between lattices demonstrates a substantially higher resistance to the Li^+ transport than a "thick" interface with a smooth, gradual transition (Fig. 6c).

Additionally, the lattice mismatch results in the emergence of a nano-sized double-layer charged arrangement, in which the appearance assumes the formation of Li-ions depleted layer; this structure also presents an obstacle for Li-ions trans-interface transport [86]. The presented consideration provides an additional conceptual basis for improvement of the inter-grain conductivity by sintering aid introduction; their implementation is favouring the appearance of seamless, gradual, and smooth grain interfaces increasing the inter-grain conductivity [86, 87].

Stability of the Li.$^+$-NASICON-ceramics in contact with electrode materials

The state of SSE/cathode and SSE/anode interfaces is the important aspect of ASSLIB design.

Stability toward Li-metal anode The most developed NASICONs with the highest Li^+ conductivities are LATP and LAGP; theoretically calculated values of the reduction potentials are 2.17 V (vs. Li/Li^+) for LATP and 2.70 V (vs. Li/Li^+) for LAGP [88], whereas the experimentally

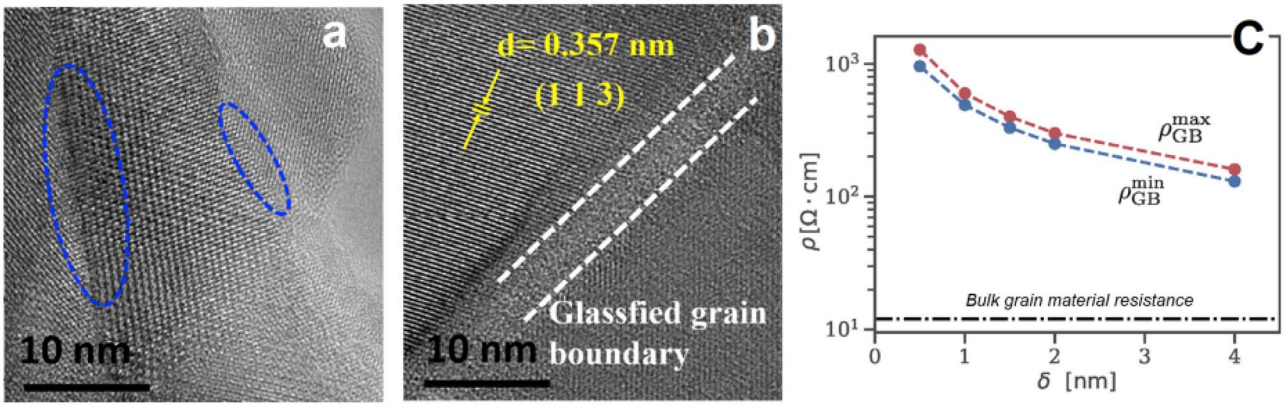

Fig. 6 (**a**) HRTEM image of $Li_{1.3}Al_{0.3}Ti_{1.7}(PO_4)_3$ ceramic sample; grain boundary is blue-circled; (**b**) HRTEM image of $Li_{1.3}Al_{0.2}B_{0.1}Ti_{1.7}(PO_4)_3$ ceramic sample (B is glass-former); grain boundary is marked with white dash corridor (reproduced with permission from [82]); (**c**) theoretical estimate of the resistance (ρ) to Li^+ transport through misaligned/distorted grain boundary depending of the thickness (δ) if the distorted layer (reproduced with permission from [82])

determined values are somehow different, namely, 2.65 V (vs. Li/Li^+) for LATP and 1.85 V (vs. Li/Li^+) for LAGP [89]. In any case, this suggests that LATPs and LAGPs are not stable in contact with Li-metal anode. The first reaction step is the local reduction of Ti^{4+} to Ti^{3+} and formation of the areas with electronically conductive phase $Li_3Al_xTi_{2-x}(PO_4)_3$; this phase is less dense than the original LATP phase. The generated wedging stresses initiate cracking of the LATP matrix, and the cracks compromise Li^+ conductivity. Since $Li_3Al_xTi_{2-x}(PO_4)_3$ phase is electronically conductive, the SSE reduction continues at the second step of the process, and the reaction products precipitate onto SSE/Li interface [90]. A similar two-step chemomechanical process of the interface degradation takes place at the LAGP/(Li-metal) boundary. The films, which form onto Li/LATP and Li/LAGP interfaces, contain P, $LiTiPO_5$, $AlPO_4$, and Li_3PO_4, and Ge, GeO_2, $Li_4P_2O_7$, and $AlPO_4$ correspondingly; the films demonstrate mixed ion-electronic conductivity, and thus, they are not passivated [88], becoming thicker with time, which results in instability of SSE/anode interface and compromises the interface conductivity. The apparent solution is the introduction of a protecting buffer layer between Li-anode and LATP/LAGP [91, 92].

While the above deliberation distinctly suggests that a preferable protective layer should be Li^+-conductive but electronically insulating, recently, some relatively efficient metallic protective buffer layers for LATP/LAGP and Li-metal anode interface were reported:

✓ It was reported that 30-nm Cr protective layer substantially increased the cycle life of Li/Cr/LAGP/$LiFePO_4$ (LFP) cell, up to 200 cycles [93]. The coating was thin enough for letting Li^+-ions to pass through the films easily; it does not prevent the precipitation of the LAGP decomposition products, since Cr-surface potential follows the potential of underlying Li. The precipitated product film was reported to be substantially more homogeneous and smoother than in the case of unprotected LAGP, though, and the authors relate the stability improvement with the change of interphase morphology, because unprotected film forms numerous wedges in the course of growth resulted in mechanical stress concentrations and the mechanical crumbling of the adjacent material layers accelerating SSE degradation [94, 95].
✓ The Li/Bi/LAGP/LFP cell with 20 nm Bi buffer film demonstrated stabile operation during 120 cycles [96]; the improvements were related to the formation of $LiBi_x$ alloy and the moderation of the SSE film formation at the [alloy]/[SSE] interface.
✓ The Li/Ge/LAGP/LFP cell with 60 nm Ge buffer film demonstrated stabile operation during 120 cycles [97]; the testing symmetrical Li/Ge/LAGP/Ge/Li cell demonstrated more than 100 cycles without a substantial degradation, whereas the reference Li/LAGP/Li cell revealed a noticeable degradation after 25 cycles.

Second, an electronically non-conductive (mostly metal oxide) protective buffer layer between LATP/LAGP and Li-anode was employed for the interface protection; the employed films were thin enough for Li^+-ions passing through the layer and were inert toward LATP/LAGP for moderating the interface reactions. It is noteworthy that these buffer films also alleviate dendrite development, because the anode dendrite growth is related to the electronic conductivity of SSEs [98]. Some examples for SSEs with buffer layers are listed below:

✓ The Li/ZnO/$Li_{1.4}Al_{0.4}Ti_{1.6}(PO_4)_3$/LFP cell with ZnO buffer layer (≈200 nm thick) operated during 200 cycles without noticeable degradation [99].
✓ The Li/ZnO/LAGP/LFP cell with ZnO buffer layer (≈50 nm thick) showed a good capacity retention after 100 cycles (0.5 C) [100]
✓ The Li/Al_2O_3/LATP/Al_2O_3/Li cell with Al_2O_3 buffer layer (≈15 nm thick, 150 ALD cycles) showed a good capacity retention after 300 cycles [101].
✓ The Li/Al_2O_3-ZnO/LATP/LFP cell with Al_2O_3–ZnO buffer layer (≈57 nm thick, Zn/Al at. ratio 25) showed a good capacity retention during 50 cycles (0.1 C) [102]
✓ The LFP/LATP/BN/Li cell retained 96.6% of initial capacity after 500 cycles for 70 days; BN coating was a highly defective polycrystalline film 5–10 nm thick [103].

While LATP and LAGP SSEs are the most extensively studied NASICON-type SSE because of their outstandingly high Li^+ conductivity, the reduction of Ti^{+4} and Ge^{+4} on contact with lithium proves itself as the immanent feature of LATP and LAGP [104]. From the electrochemical point, the phenomenon causes the degradation of LATP/(Li-anode) and LAGP/(Li-anode) interfaces because the products of the SSE reduction exhibit mixed electronic–ionic conduction. This circumstance draws the attention to zirconium-based NASICONs ($LiZr_2(PO_4)_3$, LZP). The rhombohedral modification of LZP (LZP is a polymorph material [105, 106]) has reduction potential of 2.20 vs. Li^+/Li [107], so a film appears onto LZP/Li interface upon cycling. According to the phase equilibria diagram, the film is expected to be made from such passivating film-forming materials such as Li_2O, Li_3P, Li_3PO_4, and $Li_6Zr_2O_7$ [108]; it was reported that the film was composed of Li_3P and Li_8ZrO_6 compounds and that it conducts Li^+-ions and passivates the interface against further reactions having a stable resistance upon cycling [109].

It is noteworthy that Li^+-ion mobility is inherently less in the un-doped LZP than in LGP or LTP [110], so the

improvement of LZP conductivity turns to be an important condition for development of [Li/LZP/…]-type ASSLIB configurations. Up to now, the highest reported conductivity of un-doped LZP is 1.8×10^{-4} S/cm (80 °C) [111]. Doping LZP delivered a substantial improvement of the SSE conductivities; the reported conductivity of Ca-doped LZP ($Li_{1.667}Ca_{0.333}Zr_{1.667}(PO_4)_3$, LCZP) is 25×10^{-3} S/cm, and the reported conductivity of Mg-doped LZP ($Li_{1.667}Mg_{0.333}Zr_{1.667}(PO_4)_3$, LMZP) is 19×10^{-3} S/cm (at room temperature). Such high Li^+-ion conductivities of LCZP and LMZP were attributed to the excess of Li^+-ions in the transport pathways and the highly distorted LiO_x polyhedrons [108].

Stability toward ASSLIB cathode materials

Calculated oxidation potentials are 4.21 V for LATP and 4.27 V (vs. Li/Li^+) for LAGP [88]; the experimentally determined values are in some way different, namely, 4.6 V (vs. Li/Li^+) for LATP and 4.9 V (vs. Li/Li^+) for LAGP [89]. In any case, CVs demonstrate the lack of oxidation current up to 5 V [112] (vs. Li/Li^+) for LATP and 6 V [113, 114] (vs. Li/Li^+) for LAGP, possibly because of kinetically sluggish reactions, so these SSEs are expected to be electrochemically stabile at cathode interfaces, and NASICON SSEs are the most cathodic stable among other classes of SSEs [115]. Regarding chemical stability, LATP is thermodynamically stable in contact with $LiFePO_4$, but not in contact with such common cathode materials as $LiMn_2O_4$ (LMO), $LiCoO_2$ (LCO), and $LiNi_{1/3}Co_{1/3}Mn_{1/3}O_2$ (NCM) [116]. It was demonstrated that only insignificant number of insulating phases appears on sintering at $Li_3V_2(PO_4)_3$/LAGP [117, 118], at $LiCoPO_4$/LAGP [119], at $Li_3Fe_2(PO_4)_3$/LATP [120], and (expectably) at LATP/LFP [121] interfaces.

It should be underscored the impact of ASSLIB-compacting technique on the appearance of deleterious non-conductive films in-between SSE and cathode materials. There is a clear dichotomy between the requirements of intimate contacting of SSEs and cathode material grains and the SSE-cathode material reactivity: On one hand, the rate of reactions at the SSE/(cathode material) interfaces is often insignificantly small at room and near-room temperatures even if the reactions are thermodynamically favourable, but the reactions seriously accelerate at elevated temperatures during SSEs/cathodes sintering [122]; on the other hand, a common approach for achieving such contact is to implement an elevated sintering temperature.

One of the solutions is a scrupulous choice of the optimal thermotreatment of the SSE/(cathode active material) joints; the fairly high conductive LATP/LCO [123, 124] and LATP/$LiNi_{0.8}Co_{0.1}Mn_{0.1}O_2$ [125] joints were prepared in this way. A more far-reaching way is to modify the technique of SSE/(cathode material) connection circumventing classical thermal sintering, resorting to flash sintering [126] and to spark plasma sintering [127]; up to now, the morphology and properties LAGP/$Li_3V_2(PO_4)_3$ [117], LATP/$LiCoPO_4$ [128], and LAGP/$LiFePO_4$ [129] SSE/(cathode active material) composites prepared by SPS were reported.

There is one more important feature of the implementation of high-temperature sintering for combining SSEs and cathode materials, namely, the prepared SSE/(cathode material) composite should be cooled down to the room temperature after sintering, and mechanical stresses emerge if the coefficients of thermal expansion (CTE) of the cathode active material and CTE of the corresponding SSE are different. These stresses may develop into cracks and delamination-type defects, and this aspect is devastating for mechanical strength and conductivity of the ASSLIB-related cathode/SSE composite [130]. The fundamental solution of the problem is to mate SSEs and cathode materials with CTEs, which are close to one another. In this relation, it is remarkable that the LATP/LFP couple has a fairly small thermal dilatation mismatch [131], which diminish the above stresses of the SSE/(cathode active material) composites.

Garnet-type Li-ion SSE

Conductivity of the garnet ceramics Garnet SSEs have two crystal modifications, with lattices of tetragonal and cubic symmetry correspondingly [132]. The tetragonal phase belongs to the $I4_1/acd$ space group with lattice parameters $a_t = 13.134(4)$ Å, $c_t = 12.663(8)$ Å, and $c_t/a_t = 0.9641$, and the cubic phase belongs to the Ia-3d space group with lattice parameter $a_c = 12.9827(4)$ Å. The empirical formula of a garnet is $C_3A_2B_3O_{12}$, and atom C belongs to the site Ç with oxygen dodecahedral coordination, atom A belongs to the site Ą with oxygen octahedral coordination, and atom B belongs to the site Ḅ with oxygen tetrahedral coordination [, 132, 133].

In garnet-type lithium SSE $Li_7La_3Zr_2O_{12}$ (LLZO), Ç sites are occupied by La, Ą sites are occupied by Zr, and Ḅ sites and interspaces are occupied by Li [144]. Now, the main difference in between t-LLZO and c-LLZO is the Li occupancy; c-LLZO only has two types of occupied positions for Li-ions (Li^1-tetrahedral void 24d, Li^2-eccentric octahedral gap 96 h) and the tetragonal phase; there are three Li occupancies (Li^1-tetrahedral void 8a, Li^2-regular octahedral gap 16f, Li^3-eccentric octahedral gap 32 g). The Li-ion conductivity depends on the arrangement and occupancy rate of lithium in the Li sub-lattice. The Li-ion positions and vacancies in cubic phase are less ordered than in the tetragonal phase, and hence, the ionic transport in a tetragonal phase is substantially more facile than in a tetragonal phase. Li^1 and Li^2 are in alternate positions in c-LLZO and

are concertedly occupied because of the repulsion between Li-ions in the positions (viz. if Li^1 position is occupied, two other adjacent Li^2 positions are vacant, and the next Li^2 positions are filled, so Li^+-ions may migrate along this path), and as the result, c-LLZO may reach a significant values, up to two–three orders of magnitude higher than conductivity of t-LLZO [132].

The issue is, though, that in the course of synthesis, a tetragonal modification of LLZO appears first, and it needs a prolonged (36 h or more) heating at temperatures 1200 °C (or higher) to convert the material into the more conductive cubic phase. A more practical way to stabilize cubic phase (c-LLZO) is to introduce atomic substitutions (commonly super-valent cations) into the garnet lattice; the c-phase stabilizing effect of such introduction was reported by many research groups. The c-phase stabilizing alien cations may be positioned in Li-sites, in La-sites, and in Zr-sites; such dopants as Al, Ga, and Ge are good for Li-site doping, Ce is good for La-site doping, and Ta, Te, Nb, Sb, W, Mo, Cr, Y, and Ti are good for Zr-site doping [132, 134, 135]. The extensive discussions on the matter may be found in [136–139].

Apropos of the highest reported value of garnet SSE ceramic conductivity, it is ~ 2×10^{-3} S/cm [140, 141]. The conductivity of garnet-based SSEs may be further improved based on the consideration that apart from other properties of the material, the conductivity depends on the concentration of moveable Li^+-ions; it has a maximum at some specific Li^+ concentrations, and the maximal value depends on a particular parameter of c-LLZO cell and on the particularities of the doping cation(s) [142]. Thus, the dopant is better not only for stabilizing the cubic phase but also for maintaining the optimal concentration of moveable Li^+-ions in the SSE. The right choice of the synthetic procedure and the multi-site dopant strategy is a promising approach for gaining the highest conductivity of c-LLZO [143]. Whereas this approach is centred on the in-grain conductivity of garnet SSE ceramics, this is in line with the recent reports, as the major part of the total conductivity of garnet SSE ceramics is the in-grain conductivity, and the inter-grain conductivity is only a small fraction of the total conductivity [144–147].

Stability of the LLZO ceramics in contact with electrode materials

Stability toward Li-metal anode Theoretically calculated LLZO reduction potential is ~ 0.05 V (vs. Li/Li^+), and the end products of LLZO reduction are supposed to be Li_2O, Zr_3O, and La_2O_3 [148]. Whereas these calculations suggest that generally LLZO is thermodynamically unstable in contact with Li-metal, practically the reduction potential insignificantly differs from [Li/Li^+] potential, and thus, the driving forces for the reactions LLZO ↔ (Li_2O, Zr_3O, La_2O_3) are very small; it was reported that the LL(Al)ZO/Li interface does not present a noticeable barrier for Li^+-ion transport [149]. The experimental observations and calculations have revealed that under this circumstance, bulk chemical LL(Al)ZO decomposition does not take place; a thin near-contact layer of LL(Al)ZO gets enriched with lithium, which results in the formation of thin (6 nm) film of the tetragonal phase t-LL(Al)ZO at the interface:

$$\underbrace{Li_{6.25}Al_{0.25}Zr_2O_{12}}_{\text{cubic}} \xrightarrow{0.7\bullet Li} \underbrace{Li_{6.95}Al_{0.25}Zr_2O_{12}}_{\text{tetragonal}}$$

The resulting thin tetragonal $Li_{6.95}Al_{0.25}Zr_2O_{12}$ film is actually "oxygen-deficient" when compared with the bulk of the SSE; the film passivates the interface being fairly Li^+-conductive and electronically insulating [150, 151] and does not present a noticeable barrier for Li^+-ion transport through the LL(Al)ZO/Li interface posing insignificant additional polarization resistance. The properties of such interface films essentially depend on the doping cations, though. Whereas the oxygen-deficient films at LL(Al)ZO/Li and LL(T)ZO/Li interfaces were found to be passivating, the film at LL(Nb)ZO/Li interface was found to be growing with cycling (i.e. it is non-protective); this feature was related to the possible electronic conductivity of the film [152].

Nevertheless, it was found that Li^+-ion transport experiences hindrance passing LLZO/Li interface in the case of a permanent cycling; the origin of this effect is that Li side of the interface undergoes morphological reformation due to the injection and accumulation of metal vacancies in the course of lithium dissolution/deposition. The process ends up with a pore formation and a local interface delamination, and the related loss of physical contacts between SSE and lithium decreases the LLZO/Li interface conductivity. It was reported that the application of a permanent pressure (40 mPa and up) to the Li/LLTO/cathode contact helps to preserve the interface conductivity [153]. The other way to prevent the interface conductivity degradation is to deposit a lithiophilic interlayer between lithium and LLZO. While such film does not present noticeable obstacle for Li^+ transport, it levels off lithium deposition/dissolution preventing vacancy formation and their accretion and emergence in the micro-scale delamination at Li/LLOZ interface [154–156]. The other important role of such interlayers is preventing dendrite formation, as dendrites start growing at Li surface at the spots with high current density [157].

Stability toward cathode materials No secondary oxide phases were found at LLZTO/LCO interface after heating the joint up to 900 °C [158] and up to 1050 °C [159],

and no secondary oxide phases were found at LL(Ba,Ta)O/LCO [160] interface at 900 °C. It was assumed that doping elements are relevant factors influencing stability of the LLZ(Me)O/LCO interfaces; secondary phases were found at LLZ(Al)O/LCO interface [161] at 700 °C and at LLZ(Si,AL)O/LCO interface even at 600 °C [162].

Whereas secondary oxide phases at LLZ(Ba,Ta)O/$LiNiO_2$ interface after heating the contact at 400 °C in air were reported in [160], no secondary oxide phases at LLZTO/$LiNiO_2$ interface were found in [158] after heating the contact up to 700 °C in air. Regarding the transformations of LLZTO/$LiNiO_2$ interface at elevated temperatures, it was reported that La_4NiLiO_8 phase forms at the interface at temperatures between 700 and 900 °C; this phase also conducts Li^+-ions; thus, it does not present an obstacle for Li^+ transport through the interface [158]. It was also suggested that the sintering in pure oxygen would suppress the appearance of secondary phases at this interface [158]. Whereas no secondary oxide phases were found at LLZTO/$LiNi_{0.94}Co_{0.06}O_2$ and LLZTO/$LiNi_{0.8}Mn_{0.1}Co_{0.1}O_2$ interfaces after heating the joint up to 800 °C in air, a noticeable Ni^{2+}/Li^+ redistribution takes place around this interface at 800 °C; the formation of secondary phases was found at the LLZTO/$LiMn_2O_4$, LLZTO/$Li_{1.2}Ni_{0.15}Mn_xCo_yO_2$, and LLZ(Ba,Ta)O/$LiMn_2O_4$, interfaces at temperatures 400 °C and over [158, 163]. Regarding LLZTO/$LiFePO_4$ interface, the formation of secondary oxide phases on sintering at temperatures between 500 and 800 °C of the cathode material with LLZTO was reported in [164].

An introduction of a thin intermediate layer between SSE and cathode material is the most common approach for taming the secondary phase formation, moderating through interface atomic diffusion and other related processes, which are the origins of Li^+-ion transport barriers at LLZO/(cathode material) interfaces on sintering. It was reported that the introduction of a thin (7–15 nm) Nb layer improves Li^+ transport through the LLZ(Si, AL)O/$LiCoO_2$ interface [175], the introduction of 10-nm-thick Li_3PO_4 interlayer improves Li^+ transport through LLZTO/$LiNi_{0.8}Co_{0.1}Mn_{0.1}O_2$ interface [165], and the introduction of the Li_3BO_3 interlayer improves Li^+ transport through LLZ(Al)O/$LiCoO_2$ interface [161]. The complementary solutions of this problem may be found here [166].

Li^+-ion transport failure, which originates from the morphological decay of the LLZO/(cathode material) interfaces, is discussed in [33]; the source of the SSE/(cathode material) contact delamination is the volume change of cathode material in the course of Li^+ intercalation/deintercalation [31], and the cathode volume changes impose stress/strain cycles onto the contacting SSE. This cycling is deleterious to the contact integrity because LLZO is intrinsically fragile [167]. Since the delamination rates and degrees depend on the cathode expansion coefficient, the most straightforward approach is to choose a cathode material with low volume changes on lithiation [33]. Recently, two such low-expansion cathode materials with 0.02% (low-temperature phase $LiCo_{0.85}Al_{0.15}O_2$) and 2.4% (low-temperature phase $LiMn_{0.5}Ni_{0.5}O_2$) of Li^+ intercalation expansion were offered [168]; these findings are conducive to further exploration of cathode materials with low expansion coefficients on Li intercalation.

The other approach suggests the implementation of fine-grain LLZO for preparation LLZO/(cathode material) contacts. The delamination rate and degree depend on the elasticity and hardness of SSE material; these parameters differ for grain boundaries and the bulk of LLZO grains, and the ceramics with smaller grains (and higher grain boundary share) are softer than the LLZO ceramics with large grains [169]. This suggests that the implementation of fine grain LLZO ceramics may moderate stresses at the LLZO/(cathode material) interface in the course of cell cycling and thus tame the delamination and fracturing at the interface [186].

Perovskite-type Li-ion SSE

Conductivity of the perovskite ceramics ABX_3 is a formula of a typical perovskite; $\hat{A}$ cation sites are octahedral coordinated, and $\hat{B}$ cation sites are icosahedral coordinated. <A> cation sub-lattice is built with larger cations, such as Na^+, K^+, Ca^{2+} Sr^{2+}, Ba^{2+}, and La^{3+}; B cation sub-lattice is built with smaller cations, such as Sc^{3+}, In^{3+}, Al^{3+}, Sm^{3+}, Ga^{3+}, Ti^{4+}, Zr^{4+}, Hf^{4+}, Sn^{4+}, Ge^{4+}, Nb^{5+}, and Ta^{5+}; and X is oxygen for most perovskites [170].

Li-ion conducting perovskites are $\hat{A}$ site-deficient materials, and Li-ion transport takes place in <A> sub-lattice; for this end, <A> sub-lattice should be provided with Li^+ and also vacancies (i.e. <A> sub-lattice should be only partially filled). These may be achieved by:

- Providing Li^+ and vacancies by doping <A> sub-lattice with lithium; e.g. one La^{3+} can be substituted with three Li^+; thus, the formula of Li-doped lanthanum titanium oxide $La_{2/3}TiO_3$ can be written as $Li_{3x}La_{(2/3)-x}\square_{(1/3)-2x}TiO_3$, and $\square$ stands here for a vacancy.
- Providing Li^+ and vacancies by doping <A> sub-lattice with lithium and high-valence elements, e.g. $(x+y)$ of (Sr^{2+}) can be substituted with z of (Li^+) and with y of (La^{3+}), in $SrTiO_3$ perovskite; for charge balance, $z=2x-y$ and the formula $Li_{2x-y}Sr_{1-x-y}La_yTiO_3$ with different x and y values can be obtained.
- Providing Li^+ and vacancies by doping <A> sub-lattice with lithium and B-site with higher valence cations, e.g. x of (Sr^{2+}) and y of (Zr^{4+}) can be substituted with z of (Li^+) and with y of (Ta^{5+}) in $SrZrO_3$ perovskite; for charge balance, $z=2x-y$, and the formula of the perovskite with Li/Sr/$\square$ is $Li_{2x-y}Sr_{1-x}Ta_yZr_{1-y}O_3$.

Perovskite SSEs exhibit cubic, hexagonal, orthorhombic, and tetragonal types of crystal structures; Li^+ transport takes place in < A > planes (Fig. 7); the "basic" cubic structure may undergo distortion and transmutes into structures with lower symmetry depending on substitution coefficient x in the case of certain $Li_{3x}La_{(2/3)-x}\square_{(1/3)-2x}TiO_3$ SSE, on the particular doping ions and the specific thermotreatment schedule of the individual SSE material [170–175]. The planes are packed with A cations, Li^+ cations, and vacancies, and Li^+ mobility depends on the degree of disorder of the packing [176]; the disorder in the < A > planes of a cubic SSE perovskite material is higher than the disorder in the < A > planes of a tetragonal perovskite SSE material, so the conductivity of the cubic compound is higher than the conductivity of the tetragonal material [172]. Tetragonal perovskite SSEs are characterized by the presence of the alternating A cation–rich and A cation–poor plane; the A cation–rich planes are highly ordered, whereas A cation–poor planes demonstrate disordered Li/A/vacancy arrangement, so the Li^+ transport takes place mostly in A cation–poor planes of tetragonal perovskite SSE materials [170]. Regarding Li^+ transport in the < A > planes, the critical point of Li^+ pathway is the narrowness between the oxygen anions or so named "bottleneck" (Fig. 7a). The latter may be tuned by doping < A > sub-lattice with a dopant, which is favourable for cubic structure of perovskite and intended to widen the structural bottleneck [171]; it is noteworthy that the dopant ion should be chosen so that its radius is inside the stability range of Goldschmidt perovskite tolerance factor [177]. Furthermore, the doping with matching aliovalent ions may increase Li^+ concentration in the < A > sub-lattice via maintaining a charge balance; this circumstance is also favourable for enhancing Li^+ conductivity [178]. Sr is the most common A-type dopant for La substitution in LL(Me)O SSEs, its introduction results in the widening of the structural bottlenecks and increases Li^+ concentration [139, 179].

< B > sub-lattice doping also has an impact on Li^+ conductivity of perovskite SSEs [180, 181]; in this case, the effect takes place because of the variation of the activation energy of the Li^+-ions hopping. Indeed, if the $\hat{B}$-site cation B_1 is substituted for the doping cation B_2 with a lower Gibbs potential of its oxide formation, the interatomic B_2–O bond strengthens compared to the B_1–O bond strength. This weakens the competing Â–O bonds, i.e. A–O and Li–O bonds, thus decreasing the activation energy of Li^+ hopping in < A > plane [182–184]. The $\hat{B}$-site aliovalent doping also may enhance Li^+ conductivity inducing vacancies in < A > sub-lattices for maintaining the charge balance [185]. In the case of < A > and < B > sub-lattice doping combination, synergy effects could be created through such co-doping approach [186, 187].

Up to now, the highest value of perovskite Li-ion in-grain conductivity was reported for $La_{0.56}Li_{0.36}Ti_{0.97}Al_{0.03}O_3$; it is equal to $\sigma_{bulk} = 2.95 \times 10^{-3}$ S/cm [173].

However, whereas the in-grain conductivity of perovskite SSEs is quite comparable to specific conductivities of commercial organic liquid electrolytes (which are ~ 10^{-2} S/cm),

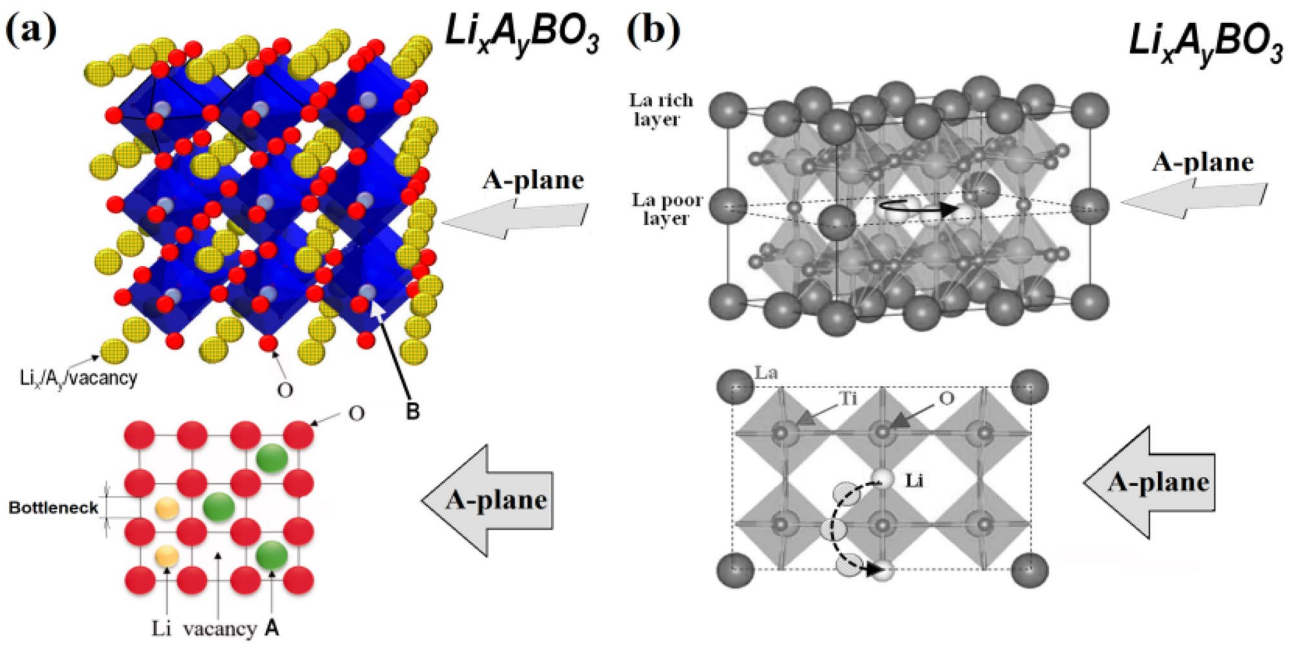

Fig. 7 Structure and schematic presentation of structure and $Li.^+$ conductivity of a perovskite oxide; (**a**) cubic perovskite (modified figure reproduced with permission from [188, 189]); (**b**) tetragonal perovskite with alternating < La-rich > and < La-loose > layers and Li conductivity in La-loose layers (modified figure reproduced with permission from [190])

the ionic conductivity of the SSE ceramic is few orders of magnitude less than the in-grain conductivity values. The cause is that ceramic body grain boundaries (GB) pose substantial restrictions to the Li^+ mobility, and in-grain-related and GB-related segments of Li^+ transport pathways in ceramic SSEs are connected in series, e.g. while the conductivity champion SSE material $La_{0.56}Li_{0.36}Ti_{0.97}Al_{0.03}O_3$ demonstrates in-grain conductivity of ~ 3×10^{-3} S/cm, the grain boundary related conductivity of this ceramic is about 2×10^{-5} S/cm. The Li^+ transporting in perovskite SSEs takes place in < A > planes by hopping through Â-site vacancies; the mismatch of < A > plane directions at the grain interfaces hinders the Li^+ transport through the GB, and such mismatch is equivalent to the appearance of a few-atom-layer-scale-thick poorly Li^+-conducting phases. This interface structure is the source of GB Li^+ transport blocking effect [191–193]. The other GB effect is related to the positive charge, which appears at the grain interfaces resulting in depleting of GB region with Li^+ and thus hindering Li^+ passage across the GBs [194, 195].

The prevailing input of GB input into the total resistance of ceramic perovskite SSE to the Li^+ transport suggests the importance of addressing the GB conductivity issue. Some efforts were focused on GB conductivity enhancement; the increasing of GB conductivity was successfully attained by suppressing Li^+ depletion at GB by the addition of lithium-rich Li_3OCl to LLTO in the course of its synthesis [196] and by slashing down the potential related to the GB positive charge; the latter was attained by LLTO Cu^{++}-doping [197]. It was also demonstrated that B̂-site cation doping increases GB conductivity by tackling the lattice mismatch issue [187, 198]. Some efforts were focused on the increasing of the ceramic grain sizes, which decreases the GB density of the ceramic SSE. Particularly, it was reported that the grain size enlargement accompanies with the increasing of the total conductivity of LLTO ceramic [199–201].

The other approach suggests the removal of the direct contacts between crystalline grains by introduction interface layers of amorphous materials, which are able to conduct Li^+; these materials may be ceramic sintering aids [202–205] or polymer electrolytes [206] and do not contain (crystalline grain)/(crystalline grain) interfaces. The authors of the cited works had reported that the substitutions of the (crystal grain)/(crystal grain) interfaces for (crystalline grain)/(amorphous Li^+ conductor) and (crystalline grain)/(polymer Li^+ conductor) interfaces result in the increase of the total conductivity of the LLTO/(amorphous Li^+ conductor) composites.

Finally, the amorphous LLTO-like compounds were examined under the assumption that while these materials do not contain crystallite grain interfaces, they would develop high Li^+ conductivity. Most of these materials were prepared by sol–gel method or PVD (pulse laser deposition or microwave sputtering) in the form of films [207–210]; these films were typically several hundred nanometers thick; and sol–gel-prepared powered amorphous LLTO ceramic also was investigated [211]. It was reported that amorphous LLTO films have higher conductivity than crystalline ceramic-type films [211]; the conductivity decreases as crystallization occurs, viz., 9.56×10^{-6} S/cm for amorphous film vs. 0.64×10^{-6} for fully crystallized film [212]. It is worth noting, however, that up to now, the best reported conductivities of crystalline LLTO ceramic SSEs supersede conductivities of the reported amorphous LLTO SSEs if the common GB resistance suppression methods (i.e. doping and adequate thermotreatment) are employed.

Stability of the LLTO ceramics in contact with electrode materials

Stability toward Li-metal anode Theoretically calculated LLTO reduction potential is 1.75 V (vs. Li/Li^+), and the end products of LLTO reduction are supposed to be $Li_4Ti_5O_{12}$, $Li_{7/6}Ti_{11/6}O_4$, and $La_2Ti_2O_7$ [88]; the potential is very close to the potential of phase decomposition (Li intercalation) [213]. This suggests that LLTO-type SSEs are not stable in contact with Li-metal anode. The formation of interfacial films during LLTO contact with metal lithium was reported; high electronic conductivity of perovskite SSE reduction is often clearly illustrated by darkening of the white body of the SSE ceramic pellet [214]. These films contained extra lithium and Ti^{+3} [215] and Ti^0 [216] species, and the electronic conductivity of the pellets increases with the time of the contact with lithium from 1.32×10^{-11} to ~ 0.12 S/cm). Such high electronic conductivity of the film proves its non-passivating nature [217]. Table 2 shows reduction potentials of some perovskite-type SSEs with B cations other than Ti. The reduction potential of LLTO makes impossible to use this SSE in direct contact not only with Li-metal and most of its alloys, but also with such Li-ion anodes as spinel $Li_4Ti_5O_{12}$ with voltage plateau of 1.5 V vs. Li/Li^+. SSEs with other tested B cations also reduce in contact with metal lithium, but SSEs with such B cations as Ta, Zr, and Hf are stable in contact with $Li_4Ti_5O_{12}$ anode.

Theoretically, $La_{2/3-x}Li_{3x}TiO_3$ is not stable in contact with metal lithium, and Ti^{+4} of LLTO is susceptible to reduction forming Ti^{+3} [88]. While such processes take place in the case of crystalline ceramic LLTO [226], amorphous modification of LLTO is stable in the contact with lithium metal [207–209]. The existing explanation implies that LLTO reduction mechanism consists of the Li-ion intercalation followed by charge transfer and forming new electronic conductive phases; Ti^{+3} ions are incorporated into lattices of these phases [226]; at the same time, the process of such

Table 2 Reduction potential of some perovskite-type SSEs (table was modified from [218])

Compounds	*B* ion	V vs. Li/Li^+	References (remarks)
$La_{2/3-x}Li_{3x}TiO_3$	Ti	1.6–1.7	[219, 220]
$La_{1/3-x}Li_{3x}NbO_3$	Nb	2.0	[221]
$(Sr,Li)(Ti,Ta)O_3$	Ti, Ta	1.5	Private communication
$Sr_{7/16}Li_{3/8}Zr_{1/4}Ta_{3/4}O_3$	Zr, Ta	1.0	[222]
$Sr_{7/16-3x/2}La_xLi_{3/8}Zr_{1/4}Ta_{3/4}O_3$ ($x=0.025$)	Zr, Ta	1.3	[223]
$Li_{3/8}Sr_{7/16}Hf_{1/4}Ta_{3/4}O_3$	Hf, Ta	1.4	[224]
$Li_{0.375}Sr_{0.4375}Hf_{0.25}Nb_{0.75}O_3$	Hf, Nb	1.4	[225]

recrystallization is hindered in the amorphous LLTO; there is no formation of conductive phases; and the reduction of LLTO is limited by several atomic layers because of the lack of charge transfer, and Li/LLTO interface passivates [207, 211]. It was reported that cells Li/(amorphous LLTO)/(different interlayers/(cathode) cells were stable for 100 cycles, and cycling performance degradation was mostly linked to the (amorphous LLTO)/(interlayer)/(cathode) junction [227].

Stability toward ASSLIB cathodes Although DFT calculated LLTO oxidation phase stability potential is obtained at ~ 3.70 V (vs. Li/Li^+), and stoichiometry stability potential of LLTO is ~ 4.46 V (vs. Li/Li^+) with end products TiO_2 and $La_2Ti_2O_7$ [88, 213], under experimental conditions, oxidation decomposition takes place with substantial over voltages against thermodynamic values, because of slow kinetics. The precession of these DFT calculated values lie in the range of 10 meV, which is a suitable self-consistent value; it is arguable that the estimations with respect to an experimental value can be better than 0.1 eV. Most often, the origin of these sluggish reactions is that the electronic conductivity of the products of oxidative decomposition is very low, and hence, the films formed by the decomposition products are passivating. Particularly passive toward oxidation are amorphous LLTO-like perovskites, which are able to withstand potentials up to 12 V (vs. Li/Li^+) [211].

This circumstance suggests that on one hand LLTO-type SSEs are expected to be relatively stable in contact with common Li-ion cell cathodes and that on the other hand a protective transition layer at the cathode/LLTO interface may be favourable for the corresponding ASSLIB stability. It was reported that while the amorphous LLTO is stable in the contact with $LiNi_{0.5}Co_{0.3}Mn_{0.2}O_2$ (NCM), the cell cycling is improved on the introduction of thin SiO_2 transition layer, so that NCO/SiO_2/LLTO/(Li-metal) may be cycled over 800 times between 4.2 and 2.7 V [227].

While calculations suggest that LLTO may decompose in contact with $LiCoO_2$ (LCO), the interface decomposition energy is very small (-5×10^{-4} eV per atom) [228], so no reaction-related transformations was found at the LCO/LLTO interface at temperatures below 300 °C [229]; material inter-diffusion and formation of Li – Ti – Co – O phase layer takes place at the LCO/LLTO interface at 700 °C, and the layer develops high resistance to Li^+ transport [230]. The amorphous LLTO coating was successfully employed for protection of sulphide SSEs against reaction with LCO [231, 232] and against reaction with $LiNi_{0.5}Co_{0.3}Mn_{0.2}O_2$ [233]; the crystalline LLTO coating was used for protection of Li_6PS_5Cl SE against reaction with $LiNi_{0.6}Co_{0.2}Mn_{0.2}O_2$ [234]. Crystalline LLTO was used as a component of a composite $LiCo_{1/3}Ni_{1/3}Mn_{1/3}O_2$ cathode of a Li-ion cell [235]. It was demonstrated that the surface coating of $LiNi_{0.815}Co_{0.15}Al_{0.035}O_2$cathode particles with LLTO increases the cycle life of the corresponding composite cathode, and the effect of crystalline LLTO coating exceeded the effect of amorphous LLTO coating [236]. The cycle life of $LiMn_2O_4$ (LMO) cathode was improved by coating LMO with the protective crystalline LLTO film; the coated LMO particles were thermos-treated at 500 °C without LMO/LLTO interface degradation [237].

Anti-perovskite type Li-ion SSE

The pioneering work of Zhao and Daemen [238] generated much interest to anti-perovskite SSEs. While anti-perovskites have a perovskite ABX_3 crystal lattice, its structure mirrors the perovskites SSE in a sense that in anti-perovskite A and B sites are occupied by anions and X sites are occupied by a cation (Fig. 8a); correspondingly, X cations form sub-lattice composed of the vertex-sharing octahedral. Although an anti-perovskite theoretically is expected to develop cubic structure, anti-perovskites also demonstrate tetragonal, orthorhombic, rhombohedral, and hexagonal phases, depending on ambient conditions (temperature, pressure) and the exact material compositions [239].

Conductivity of the anti-perovskite ceramics

Regarding Li^+-conductive SSEs, X cations are to be Li^+, and Li^+ transport in such lattice takes place along the octahedron edges, so the corollary to this circumstance is that

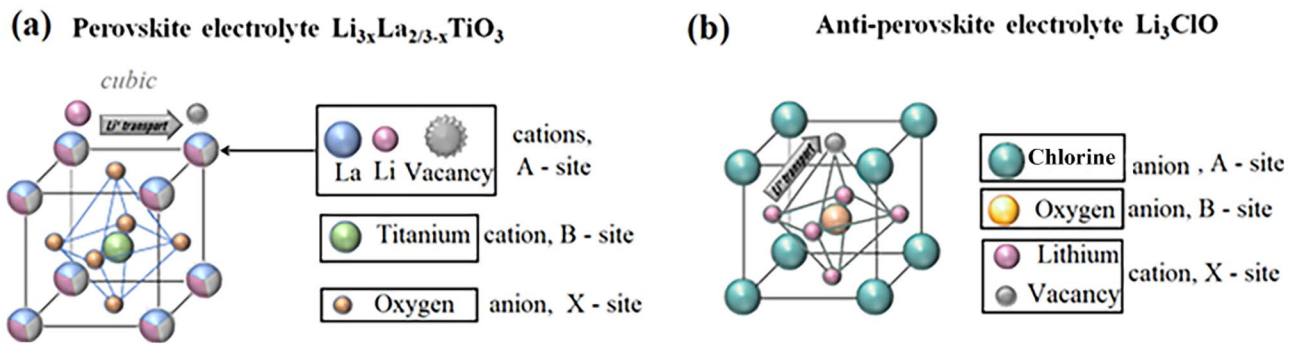

Fig. 8 Perovskite SSE and anti-perovskite SSE structures and mechanisms of Li-ion conductivities

Li^+ conductivity of the perfect anti-perovskite is very low [240–244], and sine qua non for Li^+ hopping is the presence of a vacancy (defect) in the nearby position in the cation sub-lattice (Fig. 8b). Up to now, the most investigated anti-perovskite SSE is Li_3OCl, which is considered as a model of anti-perovskite SSEs; with the reference to the Li_3OCl material, such defect suggests the simultaneous absence of the Li^+ cation and the Cl^- anion; this is a Schottky-type defect. Generally, interstitial Li^+-ions (Frenkel defects) also may move across the anti-perovskite lattice, but usually, the activation energy for the interstitial Li^+ hopping is substantially larger than for Li^+ hopping along the octahedron edges; it is also quite possible to consider such Li^+ transport as the movement of negatively charged Li-ion vacancies in the opposite direction [242]. The corollary to this circumstance is that Li^+ conductivity of the anti-perovskite with the perfect crystal lattice is very low [240–242]. Since the concentration of the intrinsic Schottky and Frenkel defects inside the anti-perovskite material ("degree of imperfectness") depends on peculiarities the synthetic procedures and characteristics of the following thermotreatment, the conductivity of SSEs also depends on these factors; e.g. the conductivity of Li_3OCl anti-perovskite SSE prepared in [238] was 0.85×10^{-3} S/cm at room temperature.

Li_3OCl doping was investigated in line with the above considerations [245]; the substitution of lithium for alkali-earth (AE) elements (supervalent doping) results in the formation of extra Li^+-vacancies in the cation sub-lattice of the matrix anti-perovskite, and the increase of the Li^+-vacancy concentration suggests the improvement of the conductivity of the resulting $Li_{3-2x}(AE)_xOCl$ material; the issue is the pairing of dopant and the corresponding Li^+-vacancy, and the dopant–vacancy binding diminishes the charge carrier (vacancy) mobility compromising $Li_{3-2x}(AE)_xOCl$ conductivity [246]; it was demonstrated that the $Li_{3-2x}Mg_xOCl$ is expected to have the highest conductivity since [Mg^{+2}-vacancy] pair has the smallest binding energy compared to [Ca^{+2}-vacancy], [Sr^{+2}-vacancy], and [Ba^{+2}-vacancy] pairs; the ionic radii similarity ($Mg^{+2}=0.72$ Å and $Li^+=0.76$ Å) was cited as the origin of the circumstance [247, 248]. Braga et al. claimed the preparation of highly conductive glassy $Li_{2.99}Mg_{0.005}OCl$, $Li_{2.99}Ca_{0.005}OCl$, $Li_{2.99}Sr_{0.005}OCl$, and $Li_{2.99}Ba_{0.005}ClO$ materials, and the conductivity of glassy $Li_{2.99}Ba_{0.005}OCl$ was reported 25 mS/cm at 25 °C [249]; later, the same authors announced preparation of $Li_{2.99}Ca_{0.005}OCl$ with conductivity 0.28 mS/cm of at 44 °C [250]; the experimental strategies of these works were contested, though. Namely, it was very probably that the reported compounds contain uncontrollable share of hydroxyl-modified compounds like $Li_{1.99}Ba_{0.005}(OH)Cl$ and also uncontrollable amount of a well-known Li^+ conductor $LiCl{\cdot}xH_2O$ [251]; these facts may explain high conductivity of the reported SSEs.

The issue of the additional concern on the matter is that the reported conductivity of Ca-doped Li_3ClO is substantially lower than the reported conductivity of Ba-doped Li_3ClO, whereas the [Ba^{+2}-vacancy] pair interaction energy is substantially higher than [Ca^{+2}-vacancy] [248], which suggests lower conductivity of Ba-doped material. It is also noteworthy that the theoretical insight on the current flow process in the amorphous Li_3ClO reveals that the Li^+-ion transference number t^{Li^+} is markedly below unity lying in the interval $0.83 < t^{Li^+} < 0.88$ depending on the temperature.

The Li_3OCl B-site doping, i.e. fluorine substitution for oxygen decreases the conductivity, because of high [F^- vacancy] binding energy; in other words, the introduction of F^- instead of O^{-2} results in interstitial Li^+, which is not an efficient conductor, and dopant-vacancy clusters with low mobility of current carriers (Li^+-vacancies) [248, 252]. The experimental confirmation of the effect was challenging because of the extreme hydroscopic nature of the substituted Li_3OCl material [253], so $Li_2(OH)Cl$ (OH^- polyanion at B site) and $Li_2(OH)_{1-x}F_xCl$ SSEs were prepared and compared. It was reported that the $Li_2(OH)Cl$ material has a cubic lattice at temperatures over 38 °C and the material conductivity $\sigma_{cub}\sim1.4\times10^{-3}$ S/cm at 39 °C, and the material has an orthorhombic lattice at temperatures below 38 °C and the material conductivity $\sigma_{orth}\sim1.2\times10^{-5}$S/cm at 37 °C

[254]. Fluorine substitution stabilizes the cubic lattice of $Li_2(OH)_{0.9}F_{0.1}Cl$ impelling the material $\sigma_F \sim 3.5 \times 10^{-5}$ S/cm at 25 °C [255]. Besides preserving a favourable cubic crystal structure, the fluorine B-doping results in the increase of the rotation rate of OH groups in fluorinated material [255] and the corresponding increase of Li^+ mobility [256]. The latter do not give a tangible rise to the conductivity of the material, though; the $Li_2(OH)_{0.9}F_{0.1}Cl$ conductivity was reported to be 1.9×10^{-3} S/cm at 100 °C, whereas the reported conductivities of $Li_2(OH)Cl$ at 100 °C are 3.5×10^{-3} S/cm [254] and 2.4×10^{-3} S/cm [257]. The B-site doping of $Li_2(OH)Cl$ with bromine also results in structural and conductivity changes; the introductions of fluorine and bromine both extend the stability region of a more conductive cubic crystal phase toward lower temperature area and thus modify conductivity of the doped materials in the following order: $Li_2(OH)Cl < Li_2(OH)Cl_{0.8}Br_{0.2} < Li_2(OH)_{0.9}F_{0.1}Cl < Li_2(OH)_{0.9}Br_{0.1}Cl$ [258].

Anti-perovskite SSE equivalent doping, i.e. alien halogen substitution for chlorine (A-site substitution), also was explored. It was reported that while the conductivity of Li_3OCl was 0.85×10^{-3} S/cm, $Li_3OBr_{0.5}Cl_{0.5}$ had demonstrated conductivity of 1.94×10^{-3} S/cm being prepared under the identical procedures [238]. Later, it was theoretically demonstrated that the conductivities of the Br-substituted SSEs are arranged in the order of $Li_3OBr_{0.25}Cl_{0.75} > Li_3OCl_{0.5}Br_{0\cdot5} > Li_3OCl > Li_3OBr$, and the optimal conductivity is provided by the $Li_3OBr_{0.25}Cl_{0.75}$ compound, in which conductivity is expected to be 30% higher than the conductivity of $Li_3OCl_{0.5}Br_{0.5}$. The result was explained in the way that Br^- introductions distort SSE lattice (Br^- and Cl^- size mismatch, $<Br^-> = 1.96$ Å, $<Cl^-> = 1.81$ Å) creating fast migration paths in the anti-perovskite structure, but an excess of Br results in would lead to clogging these channels and decreasing conductivity [259]. Similar distortion of the crystal lattice (F^- and Cl^- size mismatch, $<F^-> = 1.33$ Å, $<Cl^-> = 1.81$ Å) accompanied with increase of Li^+ mobility and Li^+ conductivity was demonstrated in the case of fluorine substitution for chlorine [256].

One more approach suggests the introduction of dopants, which generates Frenkel defects and distorts the crystal lattice of the matrix anti-perovskite in the way that its microstructure turns to be favourable for charge transport by these defects. The Frenkel defect concentration may be increased by A-site supervalent doping. This may be done by O^- substitution for Cl^- forming $Li_{3+x}O(Cl_{1-x}O_x)$ SSE material [260], but the calculations demonstrate that the Coulombic attraction toward the A-site oxygen restricts the mobility of the Li^+ interstitials forming $Li^+_{Frenkel} \cdots O^-_{A-site}$ couple with a markedly high binding energy (~0.66 eV); at the same time, the A-site substitution of sulfur for chlorine does not present that disadvantage, and the $Li^+_{Frenkel} \cdots S^-_{A-site}$ couple binding energy is just 0.031 eV, which suggests the substantially higher Li^+ interstitial mobility. The calculated conductivity of $Li_{3.125}O(Cl_{0.875}O_{0.125})$ was 1.286 mS/cm at 300 K [261].

It was reported that the generation of Frenkel defects may be also achieved by fluorine A-site substitution, and fluoride substitution for chlorine increased the concentration of Frenkel defects preserving the mobility of interstitial Li^+ high enough for enhancing the conductivity of Li_2OHBr on doping; conductivity of $Li_2OHBr_{0.98}F_{0.02}$ was found to be 1.1×10^{-6} S/cm vs. 0.91×10^{-6} S/cm for non-doped Li_2OHBr at 25 °C [262].

The anti-perovskite ceramic grain boundary conductivity is markedly over the bulk in-grain conductivity of the ceramic [251], so GB presents a substantial input into the total SSE ceramics resistance. Currently, the cause of this circumstance is linked to the lattice mismatch at the interfaces [263, 264], and the suggested way to increase the conductivity is to enlarge the ceramic grains: larger grains–lower GB concentration. It was demonstrated that the Li_3OCl polycrystalline ceramic can have total conductivity up to 85% of its in-grain conductivity value, and for this end, the ceramic grains should be $\gtrsim$500 nm in size [263]. It is also noteworthy that Li^+ transport along the GB is favourable if compared with the transport across GB [265]; this circumstance suggests a marked tortuosity of conductive pathways in the anti-perovskite ceramics. Having no GBs, glassy anti-perovskite ceramics are expected to demonstrate higher conductivity; indeed, it was reported that the glassy double anti-perovskite Li_6OSI_2 [266] had demonstrated a remarkable ionic conductivity of 6.15 mS/cm at 85 °C [267].

Stability of the anti-perovskite ceramics in contact with electrode materials

Stability toward Li-metal anode It is experimentally proven that such anti-perovskite SSEs as Li(OH)Cl [268], Li(OH)Br [269], LiOCl [270], $Li_{2.99}Ca_{0.005}ClO$ [249], $Li_2(OH)_{0.9}F_{0.1}Cl$, $Li_2(OH)_{0.9}Br_{0.1}Cl$ [258], Li_6OSI_2 [267], and Li_3SI [271] are stable in electrochemical cells under operation being in contact with metal lithium anode. However, calculation demonstrated that the work function of Li_3OCl is higher than the metal lithium working function; this means that the material is not in equilibrium with lithium, and free electrons are expected to stream in the SSE on contact with lithium. Nevertheless, the electron inflow does not result in the reduction of the bulk of Li_3OCl ceramic; instead, the electrons transferred to Cl^- atoms of the SSE creating a layer inside the Li_3OCl, and the layer does not propagate inside the bulk of the SSE forming a thin SEI with high Li^+-ion mobility [272]. The formation of the protecting SEIs at the SSE/Li interfaces was noted for several SEs when coupled with metallic Li at different conditions such as a stable cycling of a symmetric Li/$Li_2(OH)Cl$/Li cell under harsh conditions

(molten Li at 195 °C) [257], a stable cycling of a symmetric Li/Li_2OCl/Li cell at room temperature [270], and a stable cycling of a symmetric Li/Li_2OBr/Li cell at 60 °C [269].

Stability toward ASSLIB cathodes The experimental CVs of cells with anti-perovskite SSEs that originated from Li_3OCl demonstrate the outstanding electrochemical stability of these materials, although the thermodynamic assessment of the onset of oxidative decomposition of Li_3OCl is 2.55 V (vs. Li/Li^+) [240]. The stability of LiOCl at potentials ≤ 5 V was demonstrated in [264, 270], the stability of $Li_2(OH)_{0.9}F_{0.1}Cl$ was demonstrated at potentials ≤ 6 V and even at potentials ≤ 9 V [255], $Li_2(OH)_{0.9}Br_{0.1}Cl$ demonstrated stability at potentials ≤ 6 V [258], and $Li_{2.99}Ca_{0.005}ClO$ demonstrated stability at potentials ≤ 8 V [249]. The evidence is mixed regarding stability window of Li_2OHBr; according to Yoshikawa et al. [273], the material is stable up to 3.5 V, while the stability of the material at potentials ≤ 9 V was reported in [255]. Li_6OSI_2 demonstrated stability at potentials ≤ 5 V [267], and Li_3SI demonstrated stability at potentials ≤ 10 V [271]. The explanation of such large oxidation overvoltages may be related to slow kinetics of the SSE decomposition reactions [274].

Some anti-perovskite SSEs demonstrated comparability with common Li-ion cathode materials being tested in full cells anode/SSE/cathode. Li_3OCl film demonstrated comparability with $LiCoO_2$ cathode being cycled in [graphite/Li_3OCl/$LiCoO_2$] cell [264], Li_3SI demonstrated comparability with $LiNi_{0.6}Co_{0.2}Mn_{0.2}O_2$ cathode being cycled (over 50 cycles) in In/Li_3SI/$LiNi_{0.6}Co_{0.2}Mn_{0.2}O_2$ cell [275], and Li_2OHCl demonstrated comparability with $LiFePO_4$ being cycled (over 200 cycles) in Li/(LLZTO coated with Li_2OHCl core–shell SSE)/LFP cell.

LISICON Li-ion SSE

Conductivity of the LISICON ceramics High Li^+-ion conductivity in γ-Li_3PO_4-type oxides was first reported at the end of the 1970s; this group of oxides was named LISICON — Lithium Super Ionic Conductors [276, 277]. Current carriers in LISICON are intrinsic Frenkel defects — interstitial Li^+-ions; there are two types of metastable sites for such interstitials (*I* and *II* with the reference to Fig. 9), and the conductivity is carried out by Li^+-ion hopping via the channels formed by these metastable sites [278]. In this regard, it is worth to be noted that the conductivity of pure γ-Li_3PO_4 is fairly low and lie between 6.36×10^{-9} S/cm and 4.65×10^{-8} S/cm; expectably, the conductivity depends on the synthesis mode because it controls the defect concentration in the material [279].

The conductivity of the LISICON ($Li_{14}Zn(GeO_4)_4$, $\sigma_{LISICON}=2\times10^{-6}$ S/cm at 50 °C), which was reported in the pioneering work [277], was not impressive, though. The attempts to enhance the conductivity were focused on preparation of others but [Li_4GeO_4–Zn_2GeO_4] oxide solid solutions with LISICON structure. The idea is that cation substitution into the archetype LISICON material introduces extra Li^+ (over three per formula unit), and these lithium cations would be weakly bounded with oxygen anions (viz. would be placed at metastable sites) and thus would have higher mobility. For this end, a substantial number of binary LISICON-type oxide solid solutions were tested [280]; the best conductivity obtained in this way was reported for $Li_{3.7}Ge_{0.85}W_{0.15}O_4$, and it comprised 3.84×10^{-5} at 25 °C [281]. The approach was further extended to the solid solutions of three and more oxides with different cations forming LISICON structure; calculations demonstrated that in such LISICONs, the activation energy of Li^+ hopping may be decreased by the favourable choice of polyanion $(XO_4)^m$ groups, and so, the conductivity may be enhanced [282]. The general outline of the approach has paid off, and the SSE $Li_{3.68}(Ge_{0.6}V_{0.36}Ga_{0.04})O_4$ has demonstrated the highest LISICON conductivity of 1.5×10^{-4} S/cm at 25 °C reported up to now [283].

The input of grain boundaries into the total LISICON ceramic conductivity depends on the ceramic processing

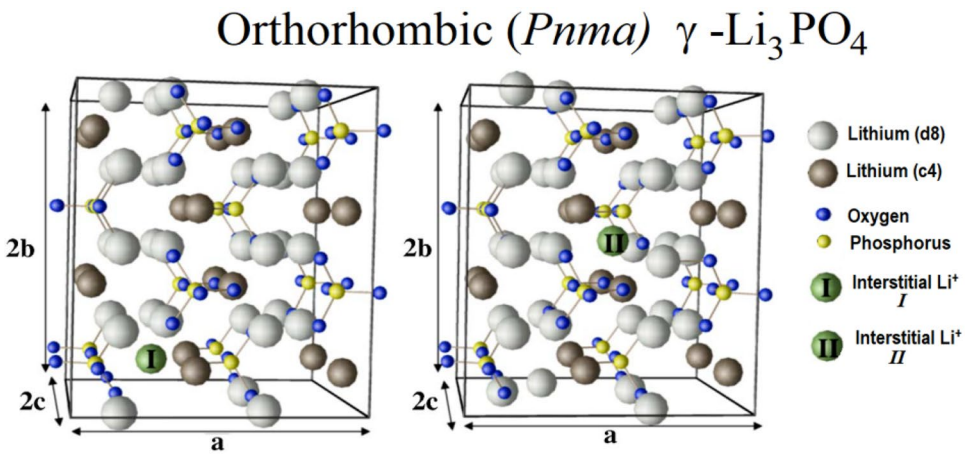

Fig. 9 Orthorhombic Pnma crystal structure of γ-Li_3PO_4 with metastable interstitial Li-ion indicated (view along the *c* axis of the primary cell); the different interstitial sites labeled *I* and *II* (reproduced with permission from [278])

mode and is often comparable with the bulk in-grain conductivity input or even smaller than the in-grain input. Regarding Li_2ZnGeO_4, it was reported that its in-grain conductivity was 3.9×10^{-7} S/cm and GB conductivity was 1.2×10^{-7} S/cm [284]; the total conductivity of $Li_{3.5}Ge_{0.75}S_{0.25}O_4$ contained mostly in-grain component being prepared under a proper pellet sintering mode [285].

Summing up, the LISICON SSE conductivities, which are reported up to now, are too low for common ambient temperature secondary battery applications and need improvements. On the other hand, many of these LISICONs fit well for high-temperature applications, such as reserve batteries, because these compounds have high thermal stability and good conductivities at elevated temperatures [286], e.g. conductivity of $Li_{14}Zn(Ge0_4)_4$ at 50 °C is just 2×10^{-6} S/cm, but it is 1.25×10^{-2} S/cm at 300 °C and 9×10^{-2} S/cm at 500 °C [277].

Stability of the LISICON ceramics in contact with electrode materials

Stability toward Li-metal anode Most LISICONs are thermodynamically unstable against metallic lithium because of Ge reduction, e.g. such LISICON as $Li_{14}Zn(GeO_4)_4$ has reduction potential 1.44 V (vs. Li/Li^+) [88].

Stability toward ASSLIB cathodes Thermodynamically calculated oxidation potential of $Li_{14}Zn(GeO_4)_4$ is 3.39 V (vs. Li/Li^+) [88]. Nevertheless, LISICON-type $Li_{3.5}Ge_{0.5}V_{0.5}O_4$ (LGVO) SSE demonstrated stability on cycling with the upper limit of 4.2 V [287].

Regarding LISICON reactivity toward common Li-ion cathode materials, no interface reaction products were detected on SPS sintering of LGVO with such cathode materials as $LiCoO_2$, $LiNi_{1/3}Mn_{1/3}Co_{1/3}O_2$, $LiNi_{0.5}Mn_{0.5}O_2$, $LiNi_{0.8}Co_{0.15}Al_{0.05}O_2$, and $Li_{1.20}Ni_{0.16}Mn_{0.55}Co_{0.09}O_2$ (450 °C for 5 min with an electric current at 400 MPa). [$LiCoO_2$/(LGVO/PEO-based electrolyte film)/(Li-metal anode)] cell and [$LiNi_{1/3}Mn_{1/3}Co_{1/3}O_2$/LGVO/(PEO-based electrolyte film)/(Li-metal anode) cell demonstrated fair cyclability and the absence of insulating layers at the cathode/(LGVO) interfaces [287]. Similar advantageous properties (no interface reactions, no interface insulating films) of LISICON SSE were reported in the case of the contact of $LiNi_{1/3}Mn_{1/3}Co_{1/3}O_2$ and the amorphous version of LISICON SSE [$0.5{\cdot}Li_{3.75}Ge_{0.75}P_{0.25}O_4 + 0.5{\cdot}Li_3BO_3$] [288].

Amorphous Li-ion SSE

Conductivity of amorphous ceramics The advantages of the oxide crystalline oxide ceramic electrolytes are outlined above, namely, these advantages are fair conductivities, good water and air stability, and comparability with metallic lithium and popular Li-ion cell cathode materials. On the other hand, the problematic aspect is a low deformability of oxide SSEs at ambient temperatures; this feature makes difficult maintaining a close contact between the cathode of ASSLIB and the SSE on battery assembling, and the poor contact results in the appearance of a high interfacial resistance between SSE and the cathode [289]. Although the common way for handling the problem is high-temperature sintering of oxide electrolytes and cathode, a low-conducting film often forms at the interfaces between many SSEs and cathode; the effect is particularly pronounced for [cathode/SSE] composite preparation [290]; besides, high-temperature sintering is a time- and energy-consuming process. In this regard, the attractive features of amorphous (glass) oxide electrolytes are their favourable mechanical properties; specifically, the amorphous SSE are soft, so the materials allow ASSLIB integration without high-temperature sintering step, while retaining the advantageous features of oxide crystalline ceramic SSEs [288, 291, 292].

Amorphous oxides (glasses) have been considered as SSEs for the last several decades [293]. Many of these materials develop very low electronic conductivities and stable in contact with metal lithium, moisture, and air [294, 295]. Most of the reported amorphous oxide SSEs demonstrate room temperature conductivities $\lesssim 10^{-5}$ S/cm [296–304], which is not high enough for common ambient temperature ASSELIBs, because the design of such cells suggests the employment of the ceramic sheets of sub-millimetre thickness. Recently, the research on a new system of amorphous oxides, $Li_2S \bullet B_2S_3 \bullet LiI \bullet SiO_2$, was reported; the conductivity of the most conductive SSE of this system (viz. $Li_{0.84}B_{0.40}Si_{0.2}O_{0.4}S_{0.84}I_{0.36}$) was found to be 2.1×10^{-3} S/cm [305], so this ceramic has the potential for being employed as the electrolyte in ambient temperature ASSELIBs.

Currently, the LiPON ($Li_xPO_yN_z$) compound can be viewed as the most investigated oxide amorphous SSE [306, 307]. While experimentally LiPON demonstrates high stability against metallic Li [308], its thermodynamic reduction potential is positive (0.68 V vs.Li/Li^+); this circumstance is linked to the formation of protection film at the interface between the SSE and Li, which inhibits further LiPON decomposition [17, 88]. The LiPON conductivity depends on synthesis and thermos-treatment conditions [309, 310], on the material content [311] and on doping with alien elements [, 17, 312]; highest reported room temperature conductivity of the doped LiPON (viz. $Li_{1.35}Si_{0.79}P_{0.21}O_{1.98}N_{0.98}$) is 2×10^{-5} S/cm [313]; reported theoretical calculations predict an incredibly high conductivity for an amorphous modification of LiPON-like compound (LiSiON), namely, $\sigma_{LiSiON} = 8.1\times10^{-3}$ S/cm [314]; in this relation, it is worth to be noted that the experimentally prepared LiSiON film (RF sputtering deposition, ~0.5 μm thick) had conductivity of 2.47×10^{-6} S/cm [315].

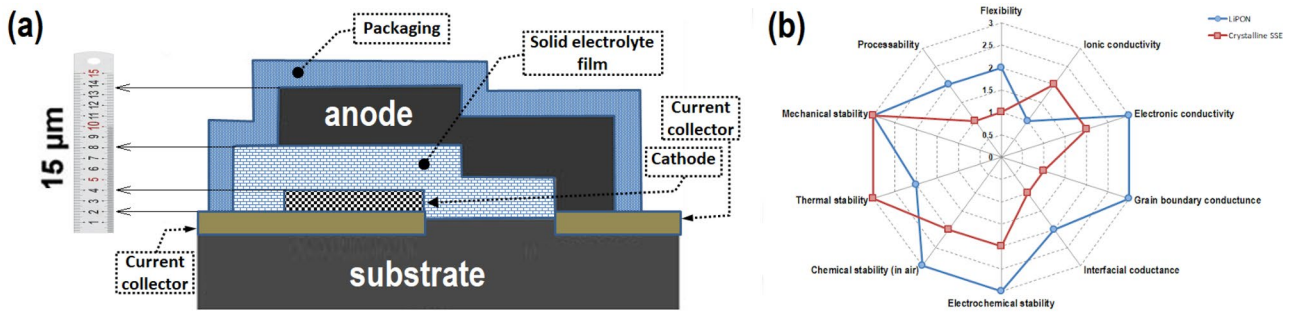

Fig. 10 (**a**) Schematics of a typical micro-ASSLIB (modified figure reproduced with permission from [320]); (**b**) radar chart comparing important features of SSEs for thin film ASSLIB (modified figure reproduced with permission from [319])

Other promising oxide amorphous SSEs belong to the system Li–V–Si–O [316]; the reported conductivity of the $Li_{1.2}V_{1.3}Si_{0.7}O_4$ film was 6.5×10^{-5} S/cm [317], which is the highest conductivity of amorphous oxide SSE reported up to now. The redox stability of LVSO does not fit well to the ASSLIB requirements; the reversible redox transformation of the in-film vanadium takes place at the potentials in the range ~ 1.0–2.7 V, and VLSO irreversibly decomposes at potentials below ~ 1.0 V. Regarding oxidation stability, VLSO was cycled without decomposition between 1.0 and 4.0 V vs. Li/Li^+ for > 20 cycles [318]. Thus, it is problematic to integrate VLSO SSE into the ASSLIB with metal lithium anode.

Applications Generally, amorphous oxide implementations are currently mostly considered in a thin-film format. First, these films fit well to thin film ASSLIB design [17, 319]. The introduction of micro-scaling devices, such as stand-alone sensor systems, medical implants and devices, labs-on-chip, and credit cards, sparks the interest to the development of electrochemical cells with thin-film architecture for powering such devices. A schematic of a typical ASSLIB micro-cell is presented in Fig. 10a.

Thicknesses of employing amorphous SSE layers commonly are few micrometres or less; this circumstance suggests the implementation of such methods of SSE application as radio frequency magnetron sputtering (RF MS), atomic layer deposition (ALD), physical vapour deposition (PVP), chemical vapour deposition (CVD), and pulsed laser deposition (PLD). Up to now, a marked number of crystalline (LISICON, LLTO, NASICON) and amorphous thin film SSEs were tested, and thin film ASSLIBs with Li-metal anodes and $LiCoO_2$ and $LiMn_2O_4$ cathodes were reported [319]; pros and cons of the crystalline and amorphous SSE films are presented in Fig. 10b, in the form of a spider web chart. The most popular amorphous thin film SSEs are LiPON films [308], although few cases of LiBON and LVSO thin film implementation also were reported [319].

Second, many crystalline SSEs are not stable in the contact with ASSLIB electrodes (viz. Li-metal anodes and/or

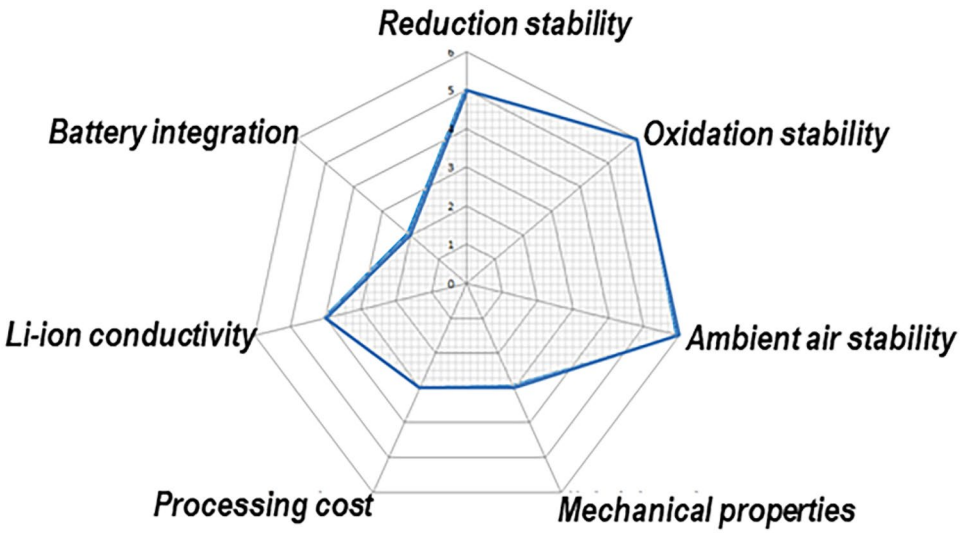

Fig. 11 Schematic presentation of the merits and demerits of oxide SSEs (modified figure reproduced with permission from [328])

cathodes) having fair conductivities; also, particular cathode materials with advantageous properties may be also prone to degradation in LIB with liquid electrolytes in the course of cell cycling. In these cases, the electrode coating with thin films of stable amorphous SSEs (mostly LiPON) may be used for preventing ASSLIB degradation [308].

✓ Even though the traditional belief was that ASSLIBs with lithium metal anode are not prone to the Li-dendrite growth during cycling, the dendrite growth at the Li/SSE interface was reported by multiple accounts; while the mechanism of the dendrite growth is still under discussion, the well-established fact is that LiPON resists the dendrite growth and that the presence of a thin LiPON layer at the Li/SSE interface suppresses the dendrite appearance [321, 322].
✓ LiPON interlayer tackles the issue of comparability of many SSEs with cathode materials on preparation and on cycling [323].
✓ LiPON coating hinders cathode material degradation in common carbonate-based LIB liquid electrolytes. A thin LiPON film (1 nm thick) substantially reduced disruptive interfacial reactions and holds up crack onset in the case of $LiCoO_2$ cathode cycling between 3 and 4.4 V [324, 325]; ~ 1-nm-thick LiPON film markedly improved cycle life of $Li_{1.2}Mn_{0.525}Ni_{0.175}Co_{0.1}O_2$ and $LiNi_{0.8}Co_{0.1}Mn_{0.1}O_2$ restraining the dissolution of transition metal from cathode [326, 327].

Conclusions

Li-ion batteries (LIB) gain leading positions in the field of energy storage across scales. The batteries are widely employing for powering portable electronics, electric vehicles, solar energy units, etc. because of high energy density, high cycle life, and high efficiency. While most LIBs offered on the market are based on liquid electrolytes now, the interest to solid electrolytes is motivated by demands for improvements of LIB safety, energy density, and manufacturability. The strengths and current weaknesses of oxide SSEs are schematically presented in the chart in Fig. 11.

Up to now, oxide SSEs demonstrated a promising data on stability toward metal lithium and on high voltage stability; these results suggest the possibility of development high energy density (batteries with Li-metal anodes) and voltage ASSLIBs. The ability of Li-dendrite growth suppression and superior thermostability of oxide SSEs impels the elevated safety to the ASSLIB with oxide SSEs. The other features such as air and moisture stability are advantageous for lowering battery production cost.

The ongoing challenges in oxide SSE research and development are:

- SSE ionic conductivity is still too low; the best reported oxide SSE conductivities are by an order of magnitude less than current commercial LIB liquid electrolytes.
- High-temperature sintering is often necessary for gaining connected and compact [cathode active material]/[oxide SSE] composite and a fair contact at the cathode/SSE assembly interface; these circumstances create manufacturing problems because of interaction between SSE and cathode materials at high temperature and also make the battery design more difficult and increase the battery processing cost.

The challenge of the development of oxide SSEs with excellent conductivity and the ability of a low-temperature processing remain to be addressed. The research continues, and new SSE materials enabling to extend the frontiers of cost, energy density, power density, cycle life, and safety are in search.

Acknowledgements S. Kundu would like to acknowledge PBC for granting PBC postdoctoral fellowship; the authors also appreciate the support of the research by the Israel National Research Centre for Electrochemical Propulsion (INREP) and the Grand Technion Energy Program (GTEP).

References

1. Funke K (2013) Solid state ionics: from Michael Faraday to green energy—the European dimension. Sci Technol Adv Mater 14(043502):1–50
2. US Patent 3,404,035 (1968) US Patent 3,413,150
3. De Rossi M, Pistoia G, Scrosati B (1969) A reversible solid-state battery with $RbAg_4I_5$ as electrolyte. J Electrochem Soc 116:1642–1645
4. Bates JB, Dudney NJ, Gruzalski GR, Zuhr RA, Choudhury A, Luck CF, Robertson JD (1992) Electrical properties of amorphous lithium electrolyte thin films. Solid State Ionics 53–56. PT 1:647–654
5. Mulmi S, Thangadurai V (2019) Solid-state electrolytes: structural approach, in Ed. R. Murugan and W. Weppner, Solid electrolytes for advanced applications: garnets and competitors; Springer. Ebook, https://doi.org/10.1007/978-3-030-31581-8
6. Goodenough JB, Park KS (2013) The Li-ion rechargeable battery: a perspective. J Am Chem Soc 135:1167–1176
7. Sheng O, Jin C, Ding X, Liu T, Wan Y, Liu Y, Nai J, Wang Y, Liu C, Tao X (2021) A decade of progress on solid-state electrolytes for secondary batteries: advances and contributions. Adv Funct Mater 31:1–25
8. Boaretto N, Garbayo I, Raj SVS, Quintela A, Li C, Casas-Cabanas M, Aguesse F (2021) Lithium solid-state batteries: state-of-the-art and challenges for materials, interfaces and processing. J Power Sources 502:229919, 1–34
9. Strauss E, Menkin S, Golodnitsky D (2017) On the way to high-conductivity single lithium-ion conductors. J Solid State Electrochem 21:1879–1905
10. Michael MS, Begam KM, Cloke M, Prabaharan SRS (2008) New NASICON type oxyanion high capacity anode, Li2Co2(MoO4)3, for lithium-ion batteries: preliminary studies. J Solid State Electrochem 12:1025–1029

11. Placke T, Kloepsch R, Dühnen S, Winter M (2017) Lithium ion, lithium metal, and alternative rechargeable battery technologies: the odyssey for high energy density. J Solid State Electrochem 21:1939–1964
12. Sivaraj P, Abhilash KP, Nalini B, et al 2021 (2020) Freestanding, high Li-ion conducting electrolytes for all-solid-state batteries. J Solid State Electrochem 25:905–917
13. Liu Z, Li G, Borodin A, et al. (2019) In situ X-ray photoelectron spectroscopy investigation of the solid. J Solid State Electrochem 23:2107–2117
14. Blanga R, Goor M, Burstein L et al (2016) The search for a solid electrolyte, as a polysulfide barrier, for lithium/sulfur batteries. J Solid State Electrochem 20:3393–3404
15. Kataoka K, Akao T, Nagata H, Nagai H, Akimoto J, Akiwatari J (2019) Development of a compact all-solid-state lithium secondary battery using a single crystal solid electrolyte — aiming to realize an oxide-based all-solid-state lithium secondary battery. Synthesiology (English edition) 12:29–40
16. Kataoka K, Nagata H, Akimoto J (2018) Lithium-ion conducting oxide single crystal as solid electrolyte for advanced Lithium battery application. Sci Rep 12:13–15
17. Lin J, Lin L, Qu S, Deng D, Wu Y, Yan X, Xie Q, Wang L, Peng D (2021) Promising electrode and electrolyte materials for high-energy-density thin-film lithium batteries. Energy and Environmental materials 5:133–156
18. Dias JA, Santagneli SH, Messaddeq Y (2020) Methods for lithium-ion NASICON preparation: from solid-state synthesis to highly conductive glass-ceramics. J Phys Chem C 124:26518–26539
19. Chen A, Qu C, Shi Y, Shi F (2020) Manufacturing strategies for solid electrolyte in batteries. Front Energy Res 8:1–18
20. DeWees R, Wang H (2019) Synthesis and properties of NASICON-type LATP and LAGP solid electrolytes. Chemsuschem 12:3713–3725
21. Yang T, Liu X, Sang L, Ding F (2013) Control of interface of glass-ceramic electrolyte/liquid electrolyte for aqueous lithium batteries. J of Power Sources 244:43–49
22. Nuernberg RB, Rodrigues ACM (2017) A new NASICON lithium ion-conducting glass-ceramic of the $Li_{1+x}Cr_x(Ge_yTi_{1-y})_{2-x}(PO_4)_3$ system. Solid State Ionics 301:1–9
23. Yan B, Zhu Y, Pan F, Liu J, Lu L (2015) $Li_{1.5}Al_{0.5}Ge_{1.5}(PO_4)_3$ Li-ion conductor prepared by melt-quench and low temperature pressing. Solid State Ionics 278:65–68
24. Cui Y, Mahmoud MM, Rohde M, Ziebert C, Seifert HJ (2016) Thermal and ionic conductivity studies of lithium aluminum germanium phosphate solid-state electrolyte. Solid State Ionics 289:125–132
25. Thokchom JS, Kumar B (2008) Composite effect in superionically conducting lithium aluminum germanium phosphate based glass-ceramic. J of Power Sources 185:480–485
26. Rahaman MN (2008) Sintering of ceramics. CRC Press, Boca Raton
27. Dashjav E, Ma Q, Xu Q, Tsai C-L, Giarola M, Mariotto G, Tietz F (2018) The influence of water on the electrical conductivity of aluminum-substituted lithium titanium phosphates. Solid State Ionics 321:83–90
28. Wang C, Liang J, Luo J, Liu J, Li X, Zhao F, Li R, Huang H, Zhao S, Zhang L, Wang J (2021) A universal wet-chemistry synthesis of solid-state halide electrolytes for all-solid-state lithium-metal batteries. Science advances 7:eabh1896 (1–9)
29. Zhu Y, Wu T, Sun J, Kotobuki M (2020) Highly conductive lithium aluminum germanium phosphate solid electrolyte prepared by sol-gel method and hot-pressing. Solid State Ionics 350:115320
30. Chen C, Jiang M, Zhou T, Raijmakers L, Vezhlev E, Wu B, Schülli TU, Danilov DL, Wei Y, Eichel R-A, Notten PHL (2021) Interface aspects in all-solid-state Li-based batteries reviewed. Adv Energy Mater 11:2003939
31. Song YB, Kwak H, Cho W, Kim KS, Jung YS, Park K-H (2022) Electrochemo-mechanical effects as a critical design factor for all-solid-state batteries. Curr Opin Solid State Mater Sci 26:100977
32. Wolfenstine J, Allen JL, Sakamoto J, Siegel DJ, Choe H (2018) Mechanical behavior of Li-ion-conducting crystalline oxide-based solid electrolytes: a brief review. Ionics 24:1271–1276
33. Barai P, Rojas T, Narayanan B, Ngo AT, Curtiss LA, Srinivasan V (2021) Investigation of delamination-induced performance decay at the cathode/LLZO interface. Chem Mater 33:5527–5541
34. He X, Zhu Y, Mo Y (2017) Origin of fast ion diffusion in superionic conductors. Nat Commun 8:15893
35. Famprikis T, Canepa P, Dawson JA, Islam MS, Masquelier C (2019) Fundamentals of inorganic solid-state electrolytes for batteries. Nat Mater 18:1278–1291
36. Dyre JC, Maass P, Roling B, Sidebottom DL (2009) Fundamental questions relating to ion conduction in disordered solids. Rep Prog Phys 72:046501
37. Chandra A, Bhatt A, Chandra A (2013) Ion conduction in superionic glassy electrolytes: an overview. J Mater Sci Technol 29:193–208
38. Tealdi C, Quartarone E, Mustarelli P (2015) In Z. Zhang and S.S. Zhang, Green energy and technology. Springer, Switzerland
39. Goodenough JB, Hong HY-P, Kafalas JA (1976) Fast Na^+-ion transport in skeleton structures. Mater Res Bull 11:203–220
40. Hagman L, Kierkegaard P (1968) The crystal structure of $NaMe^{IV}(PO_4)_3$; Me^{IV} = Ge, Ti, Zr. Acta Chem Scand 22:1822–1832
41. Aono H, Sugimoto E, Sadaoka Y, Imanaka N, Adachi G-Y (1989) Ionic conductivity of the lithium titanium phosphate (Li1 + X MXTi2 − X (PO4)3, M = Al, Sc, Y, and La) systems. J of the Electrochem Society 136:590–591
42. Jian Z, Y. – S. Hu, X. Ji, W. Chen, (2017) NASICON-structured materials for energy storage. Adv Mater 29:1601925
43. Zheng F, Kotobuki M, Song S, Lai MO, Lu L (2018) Review on solid electrolytes for all-solid-state lithium-ion batteries. J Power Sources 389:198–213
44. Yang K, Chen C, Ma J, He YB, Kang F (2021) Progress and perspective of Li1+xAlxTi2-x(PO4)3 ceramic electrolyte in lithium batteries. InfoMat 3:1195–121
45. Belous A, Kolbasov G, Kovalenko L et al (2018) All solid-state battery based on ceramic oxide electrolytes with perovskite and NASICON structure. J Solid State Electrochem 22:2315–2320
46. Rao RP, Maohua C, Adams S (2012) Preparation and characterization of NASICON type Li + ionic conductors. J Solid State Electrochem 16:3349–3354
47. Savitha T, Selvasekarapandian S, Ramya CS (2008) Structural and electrical conductivity studies of Li x AlZr[PO4]3 (x = 1.8, 2.0, 2.2), solid electrolyte for lithium-rechargeable batteries J Solid State Electrochem 12:857–860
48. Aatiq A, Ménétrier M, Croguennec L, Suard E, Delmas C (2002) On the structure of $Li_3Ti_2(PO_4)_3$. J Mater Chem 12:2971–2978
49. Arbi K, Hoelzel M, Kuhn A, García-Alvarado F, Sanz J (2013) Structural factors that enhance lithium mobility in fast-ion $Li_{1+x}Ti_{2-x}Al_x(PO_4)_3$ ($0 \le x \le 0.4$) conductors investigated by neutron diffraction in the temperature range 100–500 K. Inorg Chem 52:9290–9296
50. Cretin M, Fabry P (1999) Comparative study of lithium ion conductors in the system $Li_{1+x}Al_xA_{2-x}{}^{IV}(PO_4)_3$ with A^{IV}= Ti or Ge and $0 \le x \le 0.7$ for use as Li^+ sensitive membranes. J Eur Ceram Soc 19:2931–2940
51. Arbi K, Bucheli W, Jiménez R, Sanz J (2015) High lithium ion conducting solid electrolytes based on NASICON $Li_{1+x}Al_xM_{2-x}(PO_4)_3$

materials (M=Ti, Ge and 0≤x≤0.5). J Eur Ceram Soc 35:1477–1484
52. Monchak M, Hupfer T, Senyshyn A, Boysen H, Chernyshov D, Hansen T, Schell KG, Bucharsky EC, Hoffmann MJ, Ehrenberg H (2016) Lithium diffusion pathway in $Li_{1.3}Al_{0.3}Ti_{1.7}(PO_4)_3$ (LATP) superionic conductor. Inorg Chem 55:2941–2945
53. Wang T, Mei J, Liu J, Liao T (2021) Maximizing ionic transport of $Li_{1+x}Al_xTi_{2-x}P_3O_{12}$ electrolytes for all-solid-state lithium-ion storage: a theoretical study. J Mater Sci Technol 73:45–51
54. Akkinepally B, Reddy IN, Ko TJ, Yoo K, Shim J (2022) Dopant effect on Li^+ ion transport in NASICON-type solid electrolyte: insights from molecular dynamics simulations and experiments. Ceram Int 4:12142–12151
55. Xiao Y, Jun K, Wang Y, Miara LJ, Tu Q, Ceder G (2021) Lithium oxide superionic conductors inspired by garnet and NASICON structures. Adv Energy Mater 11:2101437
56. Xiao W, Wang J, Fan L, Zhang J, Li X (2019) Recent advances in $Li_{1+x}Al_xTi_{2-x}(PO_4)_3$ solid-state electrolyte for safe lithium batteries. Energy Storage Materials 19:379–400
57. Arbi K, Mandal S, Rojo JM, Sanz J (2002) Dependence of ionic conductivity on composition of fast ionic conductors $Li_{1+x}Ti_{2-x}Al_x(PO_4)_3$, $0 \le x \le 0.7$. A parallel NMR and electric impedance study. Chem Mater 14:1091–1097
58. Sun Z, Liu L, Lu Y, Shi G, Li J, Ma L, Zhao J, An H (2019) Preparation and ionic conduction of $Li_{1.5}Al_{0.5}Ge_{1.5}(PO_4)_3$ solid electrolyte using inorganic germanium as precursor. J Eur Ceram Soc 39:402–408
59. Nikodimos Y, Tsai MC, Abrha LH, Weldeyohannis HH, Chiu SF, Bezabh HK, Shitaw KN, Fenta FW, Wu SH, Su WN, Yang CC, Hwang BJ (2020) Al-Sc dual-doped $LiGe_2(PO_4)_3$ - a NASICON-type solid electrolyte with improved ionic conductivity. J Mater Chem A 8:11302–11313
60. Rettenwander D, Welzl A, Pristat S, Tietz F, Taibl S, Redhammer GJ, Fleig J (2016) A microcontact impedance study on NASICON-type $Li_{1+x}Al_xTi_{2-x}(PO_4)_3$ ($0 \le x \le 0.5$) single crystals. J Mater Chem A 4:1506–1513
61. Mariappan CR, Mi. Gellert, C. Yada, F. Rosciano, B. Roling, (2012) Grain boundary resistance of fast lithium ion conductors: comparison between a lithium-ion conductive Li–Al–Ti–P–O-type glass ceramic and a $Li_{1.5}Al_{0.5}Ge_{1.5}P_3O_{12}$ ceramic. Electrochem Commun 14:25–28
62. Xu Q, Tsai CL, Song D, Basak S, Kungl H, Tempel H, Hausen F, Yu S, Eichel RA (2021) Insights into the reactive sintering and separated specific grain/grain boundary conductivities of $Li_{1.3}Al_{0.3}Ti_{1.7}(PO_4)_3$. J. of Power Sources 492 : 229631
63. Ren Y, Deng H, Zhao H, Zhou Z, Wei Z (2020) A simple and effective method to prepare dense $Li_{1.3}Al_{0.3}Ti_{1.7}(PO_4)_3$ solid–state electrolyte for lithium-oxygen batteries. Ionics 26:6049–6056
64. Kotobuki M, Koishi M (2019) Influence of precursor calcination temperature on sintering and conductivity of $Li_{1.5}Al_{0.5}Ti_{1.5}(PO_4)_3$ ceramics. Journal of Asian Ceramic Societies 7:69–74
65. Yen P-Y, Lee M-L, Gregory DH, Liu W-R (2020) Optimization of sintering process on $Li_{1+x}Al_xTi_{2-x}(PO_4)_3$ solid electrolytes for all-solid-state lithium-ion batteries. Ceram Int 46:20529–20536
66. Kang J, Gu R, Guo X, Li J, Sun H, Zhang L, Jing R, Jin L, Wei X (2022) Effect of $SnO–P_2O_5–MgO$ glass addition on the ionic conductivity of $Li_{1.3}Al_{0.3}Ti_{1.7}(PO_4)_3$ solid electrolyte. Ceram Int 48:157–163
67. Kim Y-C, K. – N. Jung, J. – W. Lee, M.- S. Park, (2020) Improving the ionic conductivity of $Li_{1+x}Al_xGe_{2-x}(PO_4)_3$ solid electrolyte for all-solid-state batteries using microstructural modifiers. Ceram Int 46:23200–23207
68. Saffirio S, Falco M, Appetecchi GB, Smeacetto F, Gerbaldi C (2022) $Li_{1.4}Al_{0.4}Ge_{0.4}Ti_{1.4}(PO_4)_3$ promising NASICON-structured glass-ceramic electrolyte for all-solid-state Li-based batteries: unravelling the effect of diboron trioxide. J European Ceramic Society 42:1023–1032
69. Kwatek K, Ślubowska W, Trébosc J, Lafon O, Nowiński JL (2020) Impact of $Li_{2.9}B_{0.9}S_{0.1}O_{3.1}$ glass additive on the structure and electrical properties of the LATP-based ceramics. J Alloys Compd 820:153072
70. Odenwald P, Ma Q, Davaasuren B, Dashjav E, Tietz F, Wolff M, Rheinheimer W, Uhlenbruck S, Guillon O, Fattakhova-Rohlfing D (2022) The impact of lithium tungstate on the densification and conductivity of phosphate lithium-ion conductors. Chem Electro Chem 9
71. Vizgalov VA, Nestler T, Vyalikh A, Bobrikov IA, Ivankov OI, Petrenko V, Avdeev MV, Yashina LV, Itkis DM (2019) The role of glass crystallization processes in preparation of high Li-conductive NASICON-type ceramics. Cryst Eng Comm 21:3106–3115
72. Key B, Schroeder DJ, Ingram BJ, Vaughey JT (2012) Solution-based synthesis and characterization of Lithium-ion conducting phosphate ceramics for lithium metal batteries. Chem Mater 24:287–293
73. Liu Z, Venkatachalam S, Kirchhain H, van Wüllen L (2016) Study of the glass-to-crystal transformation of the NASICON-type solid electrolyte $Li_{1+x}Al_xGe_{2-x}(PO_4)_3$. Solid State Ionics 295:32–40
74. Yu S, Mertens A, Gao X, Gunduz DC, Schierholz R, Benning S, Hausen F, Mertens J, Kungl H, Tempel H, Eichel RA (2016) Influence of microstructure and $AlPO_4$ secondary-phase on the ionic conductivity of $Li_{1.3}Al_{0.3}Ti_{1.7}(PO_4)_3$ solid-state electrolyte. Funct Mater Lett 9:1650066
75. Schiffmann N, Bucharsky EC, Schell KG, Fritsch CA, Knapp M, Hoffmann MJ (2021) Upscaling of LATP synthesis: stoichiometric screening of phase purity and microstructure to ionic conductivity maps. Ionics 27:2017–2025
76. Thokchom JS, Kumar B (2010) The effects of crystallization parameters on the ionic conductivity of a lithium aluminum germanium phosphate glass–ceramic. J of Power Sources 195:2870–2876
77. Xu W, Qin C, Zhang S, Liang H, Lei W, Luo Z, Lu A (2021) Thermal, structural and electrical properties of fluorine-doped $Li_{3.6}Al_{0.8}Ti_{4.0}P_{7.6}O_{30-(x/2)}F_x$ (x = 0, 0.5, 1, 2) glass-ceramic electrolytes. J Alloys Compd 853:157191
78. Kwatek K, Ślubowska W, Nowiński JL, Krawczyńska AT, Sobrados I, Sanz J (2021) Electrical and structural properties of $Li_{1.3}Al_{0.3}Ti_{1.7}(PO_4)_3$—based ceramics prepared with the addition of Li_4SiO_4. Materials 14 : 5729
79. Kwatek K, Ślubowska W, Trébosc J, Lafon O, Nowiński JL (2020) Structural and electrical properties of ceramic Li-ion conductors based on $Li_{1.3}Al_{0.3}Ti_{1.7}(PO_4)_3$-LiF. J Eur Ceram Soc 40:85–93
80. Kwatek K, Ślubowska W, Ruiz C, Sobrados I, Sanz J, Garbarczyk JE, Nowiński JL (2020) The mechanism of enhanced ionic conductivity in $Li_{1.3}Al_{0.3}Ti_{1.7}(PO_4)_3 – (0.75{\cdot}Li_2O \times 0.25{\cdot}B_2O_3)$ composites. J. of Alloys and Compounds 838 : 155623
81. Bai H, Hu J, Li X, Duan Y, Shao F, Kozawa T, Naito M, Zhang J (2018) Influence of $LiBO_2$ addition on the microstructure and lithium-ion conductivity of $Li_{1+x}Al_xTi_{2-x}(PO_4)_3$ (x = 0.3) ceramic electrolyte. Ceram Int 44:6558–6563
82. Duan S, Yu J, Sun Y, Li A, Chen S, Qu K, Ding Z, Liu Z, Li Y, Huang C, Liu M, Liu J, Shi J, Huang B, Tian X, Hou S, Xie S, Liu Y, Gao P, Li J, Jin H (2020) Selective doping to relax glassified grain boundaries substantially enhances the ionic conductivity of $LiTi_2(PO_4)_3$ glass-ceramic electrolytes. J of Power Sources 449:227574
83. Kobayashi R, Nakano K, Nakayama M (2022) Non-equilibrium molecular dynamics study on atomistic origin of grain boundary

resistivity in NASICON-type Li-ion conductor. Acta Mater 226:117596
84. Nakano K, Tanibata N, Takeda H, Kobayashi R, Nakayama M, Watanabe N (2021) Molecular dynamics simulation of Li-ion conduction at grain boundaries in NASICON-Type $LiZr_2(PO_4)_3$ solid electrolytes. J Phys Chem C 125:23604–23612
85. Thokchom JS, Kumar B (2007) Ionically conducting composite membranes from the Li_2O–Al_2O_3–TiO_2–P_2O_5 glass–ceramic. J Am Ceram Soc 90:462–466
86. Luo J (2015) Interfacial engineering of solid electrolytes. Journal of Materiomics 1:22–32
87. Dai L, Wang J, Shi Z, Yu L, Shi J (2021) Influence of $LiBF_4$ sintering aid on the microstructure and conductivity of LATP solid electrolyte. Ceram Int 47:11662–11667
88. Zhu Y, He X, Mo Y (2015) Origin of outstanding stability in the Lithium solid electrolyte materials: insights from thermodynamic analyses based on first- principles calculations. ACS Appl Mater Interfaces 7:23685–23693
89. Yasmine B, Maxime R, Steeve R, Geoffroy H, Mickaël D (2021) Assessing the electrochemical stability window of NASICON-type solid electrolytes. Frontiers in Energy Research 9:682008
90. Zhu J, Zhao J, Xiang Y, Lin M, Wang H, Zheng B, He H, Wu Q, Huang JY, Yang Y (2020) Chemomechanical failure mechanism study in NASICON-type $Li_{1.3}Al_{0.3}Ti_{1.7}(PO_4)_3$ solid-state lithium batteries. Chem Mater 32:4998–5008
91. Paul PP, Chen B-R, Langevin SA, Dufek EJ, Weker JN, Ko JS (2022) Interfaces in all solid state Li-metal batteries: a review on instabilities, stabilization strategies, and scalability. Energy Storage Materials 45:969–1001
92. Tolganbek N, Serikkazyyeva A, Kalybekkyzy S, Sarsembina M, Kanamura K, Bakenov Z, Mentbayev A (2022) Interface modification of NASICON-type Li-ion conducting ceramic electrolytes: a critical evaluation. Mater Adv 3:3055–3069
93. Cortes FJQ, Lewis JA, Tippens J, Marchese TS, McDowell MT (2020) How metallic protection layers extend the lifetime of NASICON-based solid-state lithium batteries. J of the Electrochem Society 167:050502
94. Lewis JA, Cortes FJQ, Boebinger MG, Tippens J, Marchese TS, Kondekar N, Liu X, Chi M, McDowell MT (2019) Interphase morphology between a solid-state electrolyte and lithium controls cell failure. ACS Energy Lett 4:591–599
95. Krauskopf T, Richter FH, Zeier WG, Janek J (2020) Physicochemical concepts of the lithium metal anode in solid-state batteries. Chem Rev 120:7745–7794
96. Hu F, Li Y, Wei Y, Yang J, Hu P, Rao Z, Chen X, Yuan L, Li Z (2020) Construct an ultrathin bismuth buffer for stable solid-state lithium metal batteries. ACS Appl Mater Interfaces 12:12793–12800
97. Liu Y, Li C, Li B, Song H, Cheng Z, Chen M, He P, Zhou H (2018) Germanium thin film protected lithium aluminium germanium phosphate for solid-state Li batteries. Adv Energy Mater 8:1702374
98. Han F, Westover AS, Yue J, Fan X, Wang F, Chi M, Leonard DN, Dudney NJ, Wang H, Wang C (2019) High electronic conductivity as the origin of lithium dendrite formation within solid electrolytes. Nat Energy 4:187–196
99. Hao X, Zhao Q, Su S, Zhang S, Ma J, Shen L, Yu Q, Zhao L, Liu Y, Kang F, He YB (2019) Constructing multifunctional interphase between $Li_{1.4}Al_{0.4}Ti_{1.6}(PO_4)_3$ and Li metal by magnetron sputtering for highly stable solid-state lithium metal batteries. Adv. Energy Mater. 9 : 1901604
100. Ci N, Zhang L, Li J, Li D, Cheng J, Sun Q, Xi Z, Xu Z, Zhao G, Ci L (2022) In situ construction of a flexible interlayer for durable solid-state lithium metal batteries. Carbon 187:13–21
101. Liu Y, Sun Q, Zhao Y, Wang B, Kaghazchi P, Adair KR, Li R, Zhang C, Liu J, Kuo L-Y, Hu Y, Sham T-K, Zhang L, Yang R, Lu S, Song X, Sun X (2018) Stabilizing the interface of NASICON solid electrolyte against Li metal with atomic layer deposition. ACS Appl Mater Interfaces 10:31240–31248
102. Bai H, Hu J, Duan Y, Kozawa T, Naito M, Zhang J, Dong S (2019) Surface modification of $Li_{1.3}Al_{0.3}Ti_{1.7}(PO_4)_3$ ceramic electrolyte by Al_2O_3-doped ZnO coating to enable dendrites-free all-solid-state lithium-metal batteries. Ceram Int 45:14663–14668
103. Cheng Q, Li A, Li N, Li S, Zangiabadi A, Li T-D, Huang W, Li AC, Jin T, Song Q, Xu W, Ni N, Zhai H, Dontigny M, Zaghib K, Chuan X, Su D, Yan K, Yang Y (2019) Stabilizing solid electrolyte-anode interface in Li-metal batteries by boron nitride-based nanocomposite coating. Joule 3:1510–1522
104. Hartmann P, Leichtweiss T, Busche MR, Schneider M, Reich M, Sann J, Adelhelm P, Janek J (2013) Degradation of NASICON-type materials in contact with lithium metal: formation of mixed conducting interphases (MCI) on solid electrolytes. J Phys Chem C 117:21064–21074
105. Harada M, Takeda H, Suzuki S, Nakano K, Tanibata N, Nakayama M, Karasuyama M, Takeuchi I (2020) Bayesian-optimization-guided experimental search of NASICON-type solid electrolytes for all-solid-state Li-ion batteries. J Mater Chem A 8:15103–15109
106. Sudreau F, Petit D, Boilot JP (1989) Dimorphism, phase transitions, and transport properties in $LiZr_2(PO_4)_3$. J Solid State Chem 83:78–90
107. Noda Y, Nakano K, Takeda H, Kotobuki M, Lu L, Nakayama M (2017) Computational and experimental investigation of the electrochemical stability and Li-ion conduction mechanism of $LiZr_2(PO_4)_3$. Chem Mater 29:8983–8991
108. He Z, Zhang B, Zhong J, Lin Z, Pan F (2021) Tuning site energy by XO_6 units in $LiX_2(PO_4)_3$ enables high Li ion conductivity and improved stability. ACS Appl Mater Interfaces 13:50948–50956
109. H. El - Shinawi, A. Regoutz, D. J. Payne, E. J. Cussen, S. A. Corr, (2018) NASICON $LiM_2(PO_4)_3$ electrolyte (M = Zr) and electrode (M = Ti) materials for all solid-state Li-ion batteries with high total conductivity and low interfacial resistance. J Mater Chem A 6:5296–5303
110. Subramanian MA, Subramanian R, Clearfield A (1986) Lithium ion conductors in the system $AB(IV)_2(PO_4)_3$ (B = Ti, Zr and Hf). Solid State Ionics 18–19. PT 1:562–569
111. Li Y, Zhou W, Chen X, Lüc X, Cui Z, Xin S, Xue L, Jia Q, Goodenough JB (2016) Mastering the interface for advanced all-solid-state lithium rechargeable batteries. PNAS 113:13313–13317
112. Shi X, Ma N, Wu Y, Lu Y, Xiao Q, Li Z, Lei G (2018) Fabrication and electrochemical properties of LATP/PVDF composite electrolytes for rechargeable lithium-ion battery. Solid State Ionics 325:112–119
113. Xu X, Wen Z, Wu X, Yang X, Gu Z (2007) Lithium ion-conducting glass–ceramics of $Li_{1.5}Al_{0.5}Ge_{1.5}(PO_4)_{3-x}Li_2O$ (x=0.0–0.20) with good electrical and electrochemical properties. J Am Chem Soc 90:2802–2806
114. Zhang Z, Zhao Y, Chen S, Xie D, Yao X, Cui P, Xu X (2017) An advanced construction strategy of all-solid-state lithium batteries with excellent interfacial compatibility and ultralong cycle life. J Mater Chem A 5:16984–16993
115. Xiao Y, Wang Y, Bo SH, Kim JC, Miara LJ, Ceder G (2020) Understanding interface stability in solid-state batteries. Nat Rev Mater 5:105–126
116. Xiao Y, Miara LJ, Wang Y, Ceder G (2019) Computational screening of cathode coatings for solid-state batteries. Joule 3:1252–1275
117. Delaizir G, Viallet V, Aboulaich A, Bouchet R, Tortet L, Seznec V, Morcrette M, Tarascon J-M, Rozier P, Dollé M (2012) The stone age revisited: building a monolithic inorganic Lithium-ion battery. Adv Funct Mater 22:2140–2147
118. Yu S, Mertens A, Tempe H, Schierholz R, Kung H, Eichel R-A (2018) Monolithic all-phosphate solid-state lithium-ion battery with improved interfacial compatibility. ACS Appl Mater Interfaces 10:22264–22277

119. Kunshina GB, Bocharova IV, Ivanenko VI (2020) Compatibility of $LiCoPO_4$ cathode material with $Li_{1.5}Al_{0.5}Ge_{1.5}(PO_4)_3$ lithium-ion-conducting solid electrolyte. Inorg Mater 56:204–210
120. Nagata K, Nanno T (2007) All solid battery with phosphate compounds made through sintering process. J of Power Sources 174:832–837
121. Gellert M, Dashjav E, Grüner D, Ma Q, Tietz F (2018) Compatibility study of oxide and olivine cathode materials with lithium aluminum titanium phosphate. Ionics 24:1001–1006
122. Robinson JP, Kichambare PD, Deiner JL, Miller R, Rottmayer MA, Koenig GM Jr (2018) High temperature electrode-electrolyte interface formation between $LiMn_{1.5}Ni_{0.5}O_4$ and $Li_{1.4}Al_{0.4}Ge_{1.6}(PO_4)_3$. J Am Ceram Soc 101:1087–1094
123. Sakakura M, Suzuki Y, Yamamoto T, Yamamoto Y, Motoyama M, Iriyama Y (2021) Low-resistive $LiCoO_2/Li_{1.3}Al_{0.3}Ti_2(PO_4)_3$ interface formation by low-temperature annealing using aerosol deposition. Energy Technology 9 : 2001059
124. Muto S, Yamamoto Y, Sakakura M, Tian H-K, Tateyama Y, Iriyama Y (2022) STEM-EELS spectrum imaging of an aerosol-deposited NASICON-type LATP solid electrolyte and LCO cathode interface. ACS Appl Energy Mater 5:98–107
125. Yoshinari T, Koerver R, Hofmann P, Uchimoto Y, Zeier WG, Janek J (2019) Interfacial stability of phosphate-NASICON solid electrolytes in Ni-rich NCM cathode-based solid-state batteries. Appl Mater Interfaces 11:23244–23253
126. Lachal M, El Khal H, Bouvard D, Chaix J-M, Bouchet R, Steil MC (2021) Flash sintering of cationic conductive ceramics: a way to build multilayer systems. J Am Ceram Soc 104:3845–3854
127. Zhu H, Liu J (2018) Emerging applications of spark plasma sintering in all solid-state lithium-ion batteries and beyond. J of Power Sources 391:10–25
128. Okumura T, Takeuchi T, Kobayashi H (2014) Application of $LiCoPO_4$ positive electrode material in all-solid-state lithium-ion battery. Electrochemistry 82:906–908
129. Tong H, Liu J, Qiao Y, Song X (2022) Characteristics of interface between solid electrolyte and electrode in all-solid-state batteries prepared by spark plasma sintering. J of Power Sources 521:230964
130. Bucci G, Talamini B, Balakrishna AR, Chiang Y-M, Carter WC (2018) Mechanical instability of electrode-electrolyte interfaces in solid-state batteries. Phys Rev Materials 2:105407
131. Bertrand M, Rousselot S, Aymé-Perrot D, Dollé M (2021) Compatibility assessment of solid ceramic electrolytes and active materials based on thermal dilatation for the development of solid-state batteries. Mater Adv 2:2989–2999
132. Xu L, Li J, Deng W, Shuai H, Li S, Xu Z, Li J, Hou H, Peng H, Zou G, Ji X (2021) Garnet solid electrolyte for advanced all-solid-state Li batteries. Adv Energy Mater 11:2000648
133. Kataoka K, Akimoto J (2019) Lithium-ion conductivity and crystal structure of garnet-type solid electrolyte $Li_{7-x}La_3Zr_{2-x}Ta_xO_{12}$ using single-crystal. J Ceramic Society of Japan 127:521–526
134. Meesala Y, Liao Y, Jena A, Yang N, Pang W, Hu S, Chang H, Liu C, Liao S, Chen J, Guo X, Liu R (2019) An efficient multi-doping strategy to enhance Li-ion conductivity in the garnet-type solid electrolyte $Li_7La_3Zr_2O_{12}$. J Mater Chem A 7:8589–8601
135. Sodhiya A, Kumar R, Patel S, Singh A, Soni S (2020) Study of transport and structural properties of garnet structured Ce^{3+} doped $Li_7La_3Zr_2O_{12}$ electrolyte by solid state reaction method. AIP Conf Proc 2269:030073. https://doi.org/10.1063/5.0019544
136. Miara LJ, Richards WD, Wang YE, Ceder G (2015) First-principles studies on cation dopants and electrolytel cathode interphases for lithium garnets. Chem Mater 27:4040–4047
137. Stockham MP, Griffiths A, Dong B, Slater PR (2022) Assessing the importance of cation size in the tetragonal-cubic phase transition in Lithium-garnet electrolytes. Chem Eur J 28:e202103442
138. Raju MM, Altayran F, Johnson M, Wang D, Zhang Q (2021) Crystal structure and preparation of $Li_7La_3Zr_2O_{12}$ (LLZO) solid-state electrolyte and doping impacts on the conductivity: an overview. Electrochem 2:390–414
139. Jonderian A, McCalla E (2021) The role of metal substitutions in the development of Li batteries, part II: solid electrolytes. Mater Adv 2:2846–2875
140. Qin S, Zhu X, Jiang Y, Ling M, Hu Z, Zhu J (2018) Growth of self-textured Ga^{3+}-substituted $Li_7La_3Zr_2O_{12}$ ceramics by solid state reaction and their significant enhancement in ionic conductivity. Appl Phys Lett 112:113901
141. Li J, Zhang J, Zhai H, Tang X, Tan G (2022) Rapid synthesis of garnet-type $Li_7La_3Zr_2O_{12}$ solid electrolyte with superior electrochemical performance. J European Ceramic Society 42:1568–1575
142. Ramakumar S, Janani N, Murugan R (2015) Influence of lithium concentration on the structure and Li^+ transport properties of cubic phase lithium garnets. Dalton Trans 44:539–552
143. Stockham MP, Dong B, Slater PR (2022) High entropy lithium garnets – testing the compositional flexibility of the lithium garnet system. J Solid State Chem 308:122944
144. Murugan R, Ramakumar S, Janani N (2011) High conductive yttrium doped $Li_7La_3Zr_2O_{12}$ cubic lithium garnet. Electrochem Commun 13:1373–1375
145. Ohta S, Kobayashi T, Asaoka T (2011) High lithium ionic conductivity in the garnet-type oxide $Li_{7-X}La_3(Zr_{2-X}, Nb_X)O_{12}$ (X=0–2). J of Power Sources 196:3342–3345
146. Shiiba H, Zettsu N, Yamashita M, Onodera H, Jalem R, Nakayama M, Teshima K (2018) Molecular dynamics studies on the lithium ion conduction behaviors depending on tilted grain boundaries with various symmetries in garnet-type $Li_7La_3Zr_2O_{12}$. J Phys Chem C 122:21755–21762
147. Yu S, Siegel DJ (2017) Grain boundary contributions to Li-ion transport in the solid electrolyte $Li_7La_3Zr_2O_{12}$ (LLZO). Chem Mater 29:9639–9647
148. Han F, Zhu Y, He X, Mo Y, Wang C (2016) Electrochemical stability of $Li_{10}GeP_2S_{12}$ and $Li_7La_3Zr_2O_{12}$ solid electrolytes. Adv Energy Mater 6:1501590
149. Connell JG, Fuchs T, Hartmann H, Krauskopf T, Zhu Y, Sann J, Garcia-Mendez R, Sakamoto J, Tepavcevic S, Janek J (2020) Kinetic versus thermodynamic stability of LLZO in contact with lithium metal. Chem Mater 32:10207–10215
150. Ma C, Cheng Y, Yin K, Luo J, Sharafi A, Sakamoto J, Li J, More KL, Dudney NJ, Chi M (2016) Interfacial stability of Li metal–solid electrolyte elucidated via in situ electron microscopy. Nano Lett 16:7030–7036
151. Haarmann L, Rohrer J, Able K (2021) On the origin of zero interface resistance in the $Li_{6.25}Al_{0.25}La_3Zr_2O_{12}|Li^0$ system: an atomistic investigation. ACS Appl Mater Interfaces 13:52629–52635
152. Zhu Y, Connell JG, Tepavcevic S, Zapol P, Garcia-Mendez R, Taylor NJ, Sakamoto J, Ingram BJ, Curtiss LA, Freeland JW, Fong DD, Markovic NM (2019) Dopant-dependent stability of garnet solid electrolyte interfaces with lithium metal. Adv Energy Mater 9:1803440
153. Krauskopf T, Hartmann H, Zeier WG, Janek J (2019) Toward a fundamental understanding of the lithium metal anode in solid-state batteries - an electrochemo-mechanical study on the garnet-type solid electrolyte $Li_{6.25}Al_{0.25}La_3Zr_2O_{12}$. ACS Appl Mater Interfaces 11:14463–14477
154. Baniya A, Gurung A, Pokharel J, Chen K, Pathak R, Lamsal BS, Ghimire N, Bobba RS, Rahman SI, Mabrouk S, Smirnova AL, Xu K, Qiao Q (2022) Mitigating interfacial mismatch between lithium metal and garnet-type solid electrolyte by depositing metal nitride lithiophilic interlayer. ACS Appl Energy Mater 5:648–657

155. Luo W, Gong Y, Zhu Y, Li Y, Yao Y, Zhang Y, Fu K, Pastel G, Lin CF, Mo Y, Wachsman ED (2017) Reducing interfacial resistance between garnet-structured solid-state electrolyte and Li-metal anode by a germanium layer. Adv Mater 29:1606042
156. Han X, Gong Y, Fu K, He X, Hitz GT, Dai J, Pearse A, Liu B, Wang H, Rubloff G, Mo Y, Thangadurai V, Wachsman ED, Hu L (2016) Negating interfacial impedance in garnet-based solid-state Li metal batteries. Nat Mater 16:572–579
157. Neumann A, Hamann TR, Danner T, Hein S, Becker-Steinberger K, Wachsman E, Latz A (2021) Effect of the 3D structure and grain boundaries on Lithium transport in garnet solid electrolytes. ACS Appl Energy Mater 4:4786–4804
158. Yu C-Y, Choi J, Han J, Lee E, Kim J-H (2022) Phase stability of garnet solid-electrolyte interfacing with various cathodes in all-solid-state batteries. J Electrochem Soc 169:020520
159. Tsai C-L, Ma Q, Dellen C, Lobe S, Vondahlen F, Windmüller A, Grüner D, Zheng H, Uhlenbruck S, Finsterbusch M, Tietz F, Fattakhova-Rohlfing D, Buchkremer HP, Guillon O (2019) A garnet structure - based all-solid-state Li battery without interface modification: resolving incompatibility issues on positive electrodes. Sustainable Energy Fuels 3:280–291
160. Thangadurai V, Weppner W (2005) Investigations on electrical conductivity and chemical compatibility between fast lithium ion conducting garnet-like $Li_6BaLa_2Ta_2O_{12}$ and lithium battery cathodes. J of Power Sources 142:339–344
161. Park K, Yu B-C, Jung J-W, Li Y, Zhou W, Gao H, Son S, Goodenough JB (2016) Electrochemical nature of the cathode interface for a solid-state lithium-ion battery: interface between $LiCoO_2$ and garnet-$Li_7La_3Zr_2O_{12}$. Chem Mater 28:8051–8059
162. (a) Kato T, Hamanaka T, Yamamoto K, Hirayama T, Sagane F, Motoyama M, Iriyama Y (2014) In-situ Li7La3Zr2O12/LiCoO2 interface modification for advanced all-solid-state battery. J Power Sources 260:292–298; (b) Kumazaki S, Iriyama Y, Kim K-H, Murugan R, Tanabe K, Yamamoto K, Hirayama T, Ogumi Z (2011) High lithium ion conductive Li7La3Zr2O12 by inclusion of both Al and Si. Electrochem Commun 13:509–512
163. Thangadurai V, Weppner W (2005) Li6ALa2Ta2O12 (A= Sr, Ba): novel garnet-like oxides for fast lithium ion conduction. Adv Funct Mater 15(1):107–112
164. Ren Y, Liu T, Shen Y, Lin Y, Nan C-W (2016) Chemical compatibility between garnet-like solid state electrolyte $Li_{6.75}La_3Zr_{1.75}Ta_{0.25}O_{12}$ and major commercial lithium battery cathode materials. J of Materiomics 2:256–264
165. Zhao Z, Wen Z, Liu X, Yang H, Chen S, Li C, Lv H, Wu F, Wu B, Mu D (2021) Tuning a compatible interface with LLZTO integrated on cathode material for improving NCM811/LLZTO solid-state battery. Chem Eng J 405:127031
166. Li J, Wang R (2021) Recent advances in the interfacial stability, design and in situ characterization of garnet-type $Li_7La_3Zr_2O_{12}$ solid-state electrolytes based lithium metal batteries. Ceram Int 47:13280–13290
167. Yu S, Schmidt RD, Garcia-Mendez R, Herbert E, Dudney NJ, Wolfenstine JB, Sakamoto J, Siegel DJ (2016) Elastic properties of the solid electrolyte $Li_7La_3Zr_2O_{12}$ (LLZO). Chem Mater 28:197–206
168. Thackeray MM, Lee E, Shi B, Croy JR (2022) Review–from $LiMn_2O_4$ to partially-disordered Li_2MnNiO_4: the evolution of lithiated-spinel cathodes for Li-ion batteries. J of the Electrochem Society 169:020535
169. Barai P, Higa K, Ngo AT, Curtiss LA, Srinivasan V (2019) Mechanical stress induced current focusing and fracture in grain boundaries. J of the Electrochem Society 166:A1752–A1762
170. Lu J, Li Y, Y, (2021) Perovskite-type Li-ion solid electrolytes: a review. J Mater Sci: Mater Electron 32:9736–9754
171. Stramare S, Thangadurai V, Weppner W (2003) Lithium lanthanum titanates: a review. Chem Mater 15:3974–3990
172. Harada Y, Hirakoso Y, Kawai H, Kuwano J (1999) Order–disorder of the A-site ions and lithium ion conductivity in the perovskite solid solution $La_{0.67-x}Li_{3x}TiO_3$ (x=0.11). Solid State Ionics 121:245–251
173. García-Martín S, Amador U, Morata-Orrantia A, Rodríguez-Carvajal J, Alario-Franco MÁ (2009) Structure, microstructure, composition and properties of lanthanum lithium titanates and some substituted analogues. Z Anorg Allg Chem 635:2363–2373
174. Wu J, Chen L, Song T, Zou Z, Gao J, Zhang W, Shi S (2017) A review on structural characteristics, lithium ion diffusion behaviour and temperature dependence of conductivity in perovskite-type solid electrolyte $Li_{3x}La_{(2/3)-x}TiO_3$. Funct Mater Lett 10:1730002
175. Jonderian A, Ting M, McCalla E (2021) Metastability in Li–La–Ti–O perovskite materials and its impact on ionic conductivity. Chem Mater 33:4792–4804
176. Symington AR, Purton J, Statham J, Molinari M, Islam MS, Parker SC (2020) Quantifying the impact of disorder on Li-ion and Na-ion transport in perovskite titanate solid electrolytes for solid-state batteries. J Mater Chem A 8:19603–19611
177. Li Z, Yang M, Park JS, Wei SH, Berry JJ, Zhu K (2016) Stabilizing perovskite structures by tuning tolerance factor: formation of formamidinium and cesium lead iodide solid-state alloys. Chem Mater 28:284–292
178. Zhang S, Zhao H, Guo J, Du Z, Wang J, Świerczek K (2019) Characterization of Sr-doped lithium lanthanum titanate with improved transport properties. Solid State Ionics 336:39–46
179. Yang Z, Suzuki S, Tanibata N, Takeda H, Nakayama M, Karasuyama M, Takeuchi I (2020) Efficient experimental search for discovering a fast Li-ion conductor from a perovskite-type $Li_xLa_{(1-x)/3}NbO_3$ (LLNO) solid-state electrolyte using Bayesian optimization. J Phys Chem C 125:152–160
180. Huang Y, He L, Zhu X (2022) Low temperature synthesis of $Li_{0.33}La_{0.55}TiO_3$ solid electrolyte with Al^{3+} doping by a modified Pechini method. Ionics 28:1739–1751
181. Gu R, Kang J, Guo X, Li J, Yu K, Ma R, Xu Z, Jin L, Wei X (2022) Microstructure and ionic conductivity of $Li_{0.5-x}La_{0.5}(Ti_{1-x}Nb_x)O_3$ solid-state electrolytes. J Alloys Compd 896:163084
182. Thangadurai V, Weppner W (2002) Solid state lithium ion conductors: design considerations by thermodynamic approach. Ionics 8:281–292
183. Chung H-T, J. – G. Kim, H. – G. Kim, (1998) Dependence of the lithium ionic conductivity on the B-site ion substitution in $(Li_{0.5}La_{0.5})Ti_{1-x}M_xO_3$ (M=Sn, Zr, Mn, Ge). Solid State Ionics 107:153–160
184. He LX, Yoo HI (2003) Effects of B-site ion (M) substitution on the ionic conductivity of $(Li_{3x}La_{2/3-x})_{1+y/2}(M_yTi_{1-y})O_3$ (M = Al, Cr). Electrochim Acta 48:1357–1366
185. Yao R, Liu ZG, Ding ZY, Jin YJ, Cao G, Wang YH, Ouyang JH (2020) Effect of Sn or Ta doping on the microstructure and total conductivity of perovskite $Li_{0.24}La_{0.587}TiO_3$ solid electrolyte. J Alloys Compd 844:156023
186. Yu K, Jin L, Li Y, Liu G, Wei X, Yan Y (2019) Structure and conductivity of perovskite $Li_{0.355}La_{0.35}Sr_{0.3}Ti_{0.995}M_{0.005}O_3$ (M = Al, Co and In) ceramics. Ceram Int 45:23941–23947
187. Li R, Liao K, Zhou W, Li X, Meng D, Cai R, Shao Z (2019) Realizing fourfold enhancement in conductivity of perovskite $Li_{0.33}La_{0.557}TiO_3$ electrolyte membrane via a Sr and Ta co-doping strategy. J of Membrane Science 582:194–202
188. Lu J, Li Y, Ding Y (2020) Structure and conductivity of $Li_{3/8}Sr_{7/16-x}A_xZr_{1/4}Nb_{3/4}O_3$ (A = Ca, Ba) Li-ion solid electrolytes. JOM 72:3256–3261
189. Sun Y, Guan P, Liu Y, Xu H, Li S, Chu D (2019) Recent progress in lithium lanthanum titanate electrolyte towards all solid-state lithium ion secondary battery. Crit Rev Solid State Mater Sci 44:265–282

190. Mitsuishi K, Ohnishi T, Tanaka Y, Watanabe K, Sakaguchi I, Ishida N, Takeguchi M, Ohno T, Fujita D, Takada K (2012) Nazca lines by La ordering in $La_{2/3-x}Li_{3x}TiO_3$ ion-conductive perovskite. Appl Phys Lett 101:073903
191. Ma C, Chen K, Liang C, Nan C-W, Ishikawa R, More K, Chi M (2014) Atomic-scale origin of the large grain-boundary resistance in perovskite Li-ion-conducting solid electrolytes. Energy Environ, Sci 7:1638–1642
192. Lee T, Qi J, Gadre CA, Huyan H, Ko ST, Zuo Y, Du C, Li J, Aoki T, Stippich CJ, Wu R, Luo J, Ong SP, Pan X (2022) Atomic-scale origin of the low grain-boundary resistance in perovskite solid electrolytes. https://doi.org/10.48550/arXiv.2204.00091
193. Symington AR, Molinari M, Dawson JA, Statham JM, Purton J, Canepa P, Parker SC (2021) Elucidating the nature of grain boundary resistance in lithium lanthanum titanate. J Mater Chem A 9:6487–6498
194. Wu J-F, Guo X (2017) Origin of the low grain boundary conductivity in lithium ion conducting perovskites: $Li_{3x}La_{0.67-x}TiO_3$. Phys Chem Chem Phys 19:5880–5887
195. Xu L, Zhang L, Hu Y, Luo L (2022) Structural origin of low Li-ion conductivity in perovskite solid-state electrolyte. Nano Energy 92:106758
196. He X, Li S, Cao G, Hu J, Zhang J, Qiao R, Pan J, Shao G (2020) In situ atomic-scale engineering of the chemistry and structure of the grain boundaries region of $Li_{3x}La_{2/3-x}TiO_3$. Scripta Mater 185:134–139
197. Polczyk T, Zając W, Ziąbka M, Świerczek K (2021) Mitigation of grain boundary resistance in $La_{2/3-x}Li_{3x}TiO_3$ perovskite as an electrolyte for solid-state Li-ion batteries. J Mater Sci 56:2435–2450
198. Jiang Y, Huang Y, Hu Z, Zhou Y, Zhu J, Zhu X (2020) Effects of B-site ion (Nb^{5+}) substitution on the microstructure and ionic conductivity of $Li_{0.5}La_{0.5}TiO_3$ solid electrolytes. Ferroelectrics 554:89–96
199. Geng H, Lan J, Mei A, Lin Y, Nan CW (2011) Effect of sintering temperature on microstructure and transport properties of $Li_{3x}La_{2/3-x}TiO_3$ with different lithium contents. Electrochim Acta 56:3406–3414
200. Kwon WJ, H. l Kim, K.-N. Jung, W. Cho, S. H. Kim, J. – W. Lee, M. – S. Park, (2017) Enhanced Li^+ conduction in perovskite $Li_{3x}La_{2/3-x\square 1/3-2x}TiO_3$ solid-electrolytes via microstructural engineering. J Mater Chem A 5:6257–6262
201. Lu X, Zhang F, Li J (2021) The influence of lithium sources on properties of perovskite-type lithium ion conductor. J Alloy Compd 875:159887
202. Mei A, Wang X-L, Lan J-L, Feng Y-C, Geng H-X, Lin Y-H, Nan C-W (2010) Role of amorphous boundary layer in enhancing ionic conductivity of lithium–lanthanum–titanate electrolyte. Electrochim Acta 55:2958–2963
203. Zhang H, Hao S, Lin J (2017) Influence of Li_2O-B_2O_3 glass on ionic migration and interfacial properties of $La_{2/3-x}Li_{3x}TiO_3$ solid electrolyte. J Alloy Compd 704:109–116
204. Yu K, Gu R, Wu L, Sun H, Ma R, Jin L, Xu Y, Xu Z, Wei X (2018) Ionic and electronic conductivity of solid electrolyte $Li_{0.5}La_{0.5}TiO_3$ doped with LiO_2-SiO_2-B_2O_3 glass. J Alloy Compd 739:892–896
205. Salami TJ, Imanieh SH, Lawrence JG, Martin IR (2019) Amorphous glass-perovskite composite as solid electrolyte for lithium-ion battery. Mater Lett 254:294–296
206. Boyano I, Mainar AR, Blázquez JA, Kvasha A, Bengoechea M, De Meatza I, García-Martín S, Varez A, Sanz J, García-Alvarado F (2021) Reduction of grain boundary resistance of $La_{0.5}Li_{0.5}TiO_3$ by the addition of organic polymers. Nanomaterials 11:61 (1–12)
207. Ahn J-K, Yoon S-G (2005) Characteristics of amorphous lithium lanthanum titanate electrolyte thin films grown by PLD for use in rechargeable lithium microbatteries. Electrochem Solid-State Lett 8:A75–A78
208. Zheng Z, Fang H, Yang F, Liu Z-K, Wang Y (2014) Amorphous $LiLaTiO_3$ as solid electrolyte material. J Electrochem Soc 161:A473–A479
209. Lee JZ, Wang Z, Xin HL, Wynn TA, Meng YS (2017) Amorphous lithium lanthanum titanate for solid-state microbatteries. J Electrochem Soc 164:A6268–A6273
210. Zheng Z, Zhang Y, Song S, Wang Y (2017) Sol–gel-processed amorphous inorganic lithium ion electrolyte thin films: sol chemistry. RSC Adv 7:30160–30165
211. Zheng Z, Fang H-Z, Liu Z-K, Wang Y (2015) Fundamental stability study for amorphous $LiLaTiO_3$ solid electrolyte. J Electrochem Soc 162:A244–A248
212. Tan F, An H, Li N, Du J, Peng Z (2021) A study on $Li0._{33}La_{0.55}TiO_3$ solid electrolyte with high ionic conductivity and its application in flexible all-solid-state batteries. Nanoscale 13:11518–11524
213. Binninger T, Marcolongo A, Mottet M, Weber V, Laino T (2020) Comparison of computational methods for the electrochemical stability window of solid-state electrolyte materials. J of Materials Chemistry A 8:1347–1359
214. Lu J, Li Y, Ding Y (2021) Li-ion conductivity and electrochemical stability of A-site deficient perovskite-structured $Li_{3x-y}La_{1-x}Al_{1-y}Ti_yO_3$ electrolytes. Mater Res Bull 133:111019
215. Yang K, Leu I, Fung K, Hon M, Hsu M, Hsiao Y, Wang M (2008) Mechanism of the interfacial reaction between cation-deficient $La_{0.56}Li_{0.33}TiO_3$ and metallic lithium at room temperature. J Mater Res 23:1813–1825
216. Wenzel S, Leichtweiss T, Krüger D, Sann J, Janek J (2015) Interphase formation on lithium solid electrolytes—an in situ approach to study interfacial reactions by photoelectron spectroscopy. Solid State Ionics 278:98–105
217. Inaguma Y (2021) Perovskite-type lithium-ion solid electrolytes. In: Kanamura, K. (eds) Next generation batteries. Springer, Singapore, https://doi.org/10.1007/978-981-33-6668-8_18
218. Inaguma Y, Itoh M (1996) Influences of carrier concentration and site percolation on lithium ion conductivity in perovskite-type oxides. Solid State Ionics 86:257–260
219. Shan YJ, Chen L, Inaguma Y, Itoh M, Nakamura T (1995) Oxide cathode with perovskite structure for rechargeable lithium batteries. J of Power Sources 54:397–402
220. Birke P, Scharner S, Huggins RA, Weppner W (1997) Electrolytic stability limit and rapid lithium insertion in the fast-Ion-conducting $Li_{0.29}La_{0.57}TiO_3$ perovskite-type compound. J of the Electrochemical Society 144:L167–L169
221. Nakayama M, Imaki K, Ikuta H, Uchimoto Y, Wakihara M (2002) Electrochemical lithium insertion for perovskite oxides of $Li_yLa_{(1-y)/3}NbO_3$ (y = 0, 0.1, 0.25). J Phys Chem B 106:6437–6441
222. Chen CH, Xie S, Sperling E, Yang AS, Henriksen G, Amine K (2004) Stable lithium-ion conducting perovskite lithium–strontium–tantalum–zirconium–oxide system. Solid State Ionics 167:263–272
223. Lu J, Li Y (2018) Conductivity and stability of $Li_{3/8}Sr_{7/16-3x/2}La_xZr_{1/4}Ta_{3/4}O_3$ superionic solid electrolytes. Electrochim Acta 282:409–415
224. Huang B, Xu B, Li Y, Zhou W, You Y, Zhong S, Wang C-A, Goodenough JB (2016) Li-ion conduction and stability of perovskite $Li_{3/8}Sr_{7/16}Hf_{1/4}Ta_{3/4}O_3$. ACS Appl Mater Interfaces 8:14552–14557
225. Kong Y, Li Y, Lu J, Hu C (2017) Conductivity and electrochemical stability of perovskite-structured lithium–strontium–niobium–hafnium-oxide solid Li-ion conductor. J Mater Sci: Mater Electron 28:8621–8629
226. Chen CH, Amine K (2001) Ionic conductivity, lithium insertion and extraction of lanthanum lithium titanate. Solid State Ionics 144:51–57
227. Tan F, An H, Li N, Du J, Peng Z (2021) Stabilization of $Li_{0.33}La_{0.55}TiO_3$ solid electrolyte interphase layer and enhancement of cycling performance of $LiNi_{0.5}Co_{0.3}Mn_{0.2}O_2$ battery cathode with buffer layer. Nanomaterials 11:989

228. Zhu Y, He X, Mo Y (2016) First principles study on electrochemical and chemical stability of solid electrolyte–electrode interfaces in all-solid-state Li-ion batteries. J Mater Chem A 4:3253–3266
229. Chandra S, Kim Y, Vivona D, Waluyo I, Hunt A, Schlueter C, Lee JB, Shao-Horn Y, Yildiz B (2022) Thermally-driven reactivity of $Li_{0.35}La_{0.55}TiO_3$ solid electrolyte with $LiCoO_2$ cathode. J Mater Chem A 10:3485–3494
230. Xu P, Rheinheimer W, Mishra A, Shuvo SN, Qi Z, Wang H, Dongare AM, Stanciu LA (2021) Origin of high interfacial resistance in solid-state batteries: LLTO/LCO half-cells. Chem Electro Chem 8:1847–1857
231. Noh S, Kim J, Eom M, Shin D (2013) Surface modification of LiCoO2 with Li3xLa2, 3−xTiO3 for all-solid-state lithium ion batteries using Li2S–P2S5 glass–ceramic. Ceramics International 39:8453–8458
232. Zou C, Yang L, Luo K et al (2021) Ionic conductivity and interfacial stability of Li6PS5Cl–Li6.5La3Zr1.5Ta0.5O12 composite electrolyte. J Solid State Electrochem 25:2513–2525
233. Yi J, He P, Liu H, Ni H, Bai Z, Fan L-Z (2021) Manipulating interfacial stability of $LiNi_{0.5}Co_{0.3}Mn_{0.2}O_2$ cathode with sulfide electrolyte by nanosized LLTO coating to achieve high-performance all-solid-state lithium batteries. J Energy Chem 52:202–209
234. Fan Z, Xiang J, Yu Q, Wu X, Li M, Wang X, Xia X, Tu J (2022) High performance single-crystal Ni-rich cathode modification via crystalline LLTO nanocoating for all-solid-state Lithium batteries. ACS Appl Mater Interfaces 14:726–735
235. Lin X, Wang H, Du H, Xiong X, Qu B, Guo Z, Chu D (2016) Growth of lithium lanthanum titanate nanosheets and their application in Lithium-ion batteries. ACS Appl Mater Interfaces 8:1486–1492
236. Xu C-L, Xiang W, Wu Z-G, Li Y-C, Xu Y-D, Hua W-B, Guo X-D, Zhang X-B, Zhong B-H (2018) A comparative study of crystalline and amorphous $Li_{0.5}La_{0.5}TiO_3$ as surface coating layers to enhance the electrochemical performance of $LiNi_{0.815}Co_{0.15}Al_{0.035}O_2$ cathode. J Alloy Compd 740:428–435
237. Hua S, Li Y, Lai F, Zhang X, Li Q, Huang Y, Yuan X, Chen J, Wang H (2015) Enhanced electrochemical performance of $LiMn_2O_4$ cathode with a $Li_{0.34}La_{0.51}TiO_3$-coated layer. RSC Adv 5:17592–17600
238. Zhao Y, Daemen LL (2012) Superionic conductivity in lithium-rich anti-perovskites. J Am Chem Soc 134:15042–15047
239. Xia W, Zhao Y, Zhao F, Adair K, Zhao R, Li S, Zou R, Zhao Y, Sun X (2022) Antiperovskite electrolytes for solid-state batteries. Chem Rev 122:3763–3819
240. Emly A, Kioupakis E, Van der Ven A (2013) Phase stability and transport mechanisms in antiperovskite Li_3OCl and Li_3OBr superionic conductors. Chem Mater 25:4663–4670
241. Zhang Y, Zhao Y, Chen C (2013) Ab initio study of the stabilities of and mechanism of superionic transport in lithium-rich antiperovskites. Phys Rev B 87:134303
242. Mouta R, Melo MAB, Diniz EM, Paschoal CWA (2014) Concentration of charge carriers, migration, and stability in Li_3OCl solid electrolytes. Chem Mater 26:7137–7144
243. Lu Z, Chen C, Baiyee ZM, Chen X, Niu C, Ciucci F (2015) Defect chemistry and lithium transport in Li_3OCl anti-perovskite superionic conductors. Phys Chem Chem Phys 17:32547–32555
244. Wu M, Xu B, Lei X, Huang K, Ouyang C (2018) Bulk properties and transport mechanisms of a solid state antiperovskite Li-ion conductor Li_3OCl: insights from first principles calculations. J Mater Chem A 6:1150–1160
245. Dawson JA, Famprikis T, Johnston KE (2021) Anti-perovskites for solid-state batteries: recent developments, current challenges and future prospects. J Mater Chem A 9:18746–18772
246. Islam MS, Davies RA (2004) Atomistic study of dopant site-selectivity and defect association in the lanthanum gallate perovskite. J Mater Chem 14:86–93
247. Stegmaier S, Voss J, Reuter K, Luntz AC (2017) Li^+ defects in a solid-state Li ion battery: theoretical insights with a Li_3OCl electrolyte. Chem Mater 29:4330–4340
248. Clarke MJ, Dawson JA, Mays TJ, Islam MS (2021) Atomistic insights into the effects of doping and vacancy clustering on Li-ion conduction in the Li_3OCl antiperovskite solid electrolyte. ACS Appl Energy Mater 4:5094–5100
249. Braga MH, Ferreira JA, Stockhausen V, Oliveira JE, El-Azab A (2014) Novel Li_3ClO based glasses with superionic properties for lithium batteries. J Mater Chem A 2:5470–5480
250. Braga MH, Murchison AJ, Ferreira JA, Singh P, Goodenough JB (2016) Glass-amorphous alkali-ion solid electrolytes and their performance in symmetrical cells. Energy Environ Sci 9:948–954
251. Hanghofer I, Redhammer GJ, Rohde S, Hanzu I, Senyshyn A, Wilkening HMR, Rettenwander D (2018) Untangling the structure and dynamics of lithium-rich anti-perovskites envisaged as solid electrolytes for batteries. Chem Mater 30:8134–8144
252. Squires A, Dean JM, Morgan BJ (2021) Aliovalent doping strategies for enhancing ionic conductivity in Li_3OCl solid electrolytes: a first-principles assessment. https://chemrxiv.org/engage/api-gateway/chemrxiv/assets/orp/resource/item/611534d018911d675edf20e2/original/aliovalent-doping-response-and-impact-on-ionic-conductivity-in-the-antiperovskite-solid-electrolyte-li3o-cl.pdf
253. Li S, Zhu J, Wang Y, Howard JW, Lü X, Li Y, Kumar RS, Wang L, Daemen LL, Zhao Y (2016) Reaction mechanism studies towards effective fabrication of lithium-rich anti-perovskites Li_3OX (X=Cl, Br). Solid State Ionics 284:14–19
254. Wang F, Evans HA, Kim K, Yin L, Li Y, Tsai PC, Liu J, Lapidus SH, Brown CM, Siegel DJ, Chiang YM (2020) Dynamics of hydroxyl anions promotes lithium ion conduction in antiperovskite Li_2OHCl. Chem Mater 32:8481–8491
255. Li Y, Zhou W, Xin S, Li S, Zhu J, Lü X, Cui Z, Jia Q, Zhou J, Zhao Y, Goodenough JB (2016) Fluorine-doped antiperovskite electrolyte for all-solid-state lithium-ion batteries. Angew Chem Int Ed 55:9965–9968
256. Effat MB, Liu J, Lu Z, Wan TH, Curcio A, Ciucci F (2020) Stability, elastic properties, and the Li transport mechanism of the protonated and fluorinated antiperovskite lithium conductors. ACS Appl Mater Interfaces 12:55011–55022
257. Hood ZD, Wang H, Pandian AS, Keum JK, Liang C (2016) Li_2OHCl crystalline electrolyte for stable metallic lithium anodes. J Am Chem Soc 138:1768–1771
258. Lee Y-S, Jung S-Y, Ryu K-S (2021) Electrochemical stability and performance of Li_2OHCl substituted by F or Br as solid-state electrolyte. J Electrochem En Conv Stor 18:021011
259. Deng Z, Radhakrishnan B, Ong SP (2015) Rational composition optimization of the lithium-rich $Li_3OCl_{1-x}Br_x$ anti-perovskite superionic conductors. Chem Mater 27:3749–3755
260. Mouta R, Diniz EM, Paschoal CWA (2016) Li^+ interstitials as the charge carriers in superionic lithium-rich anti-perovskites. J Mater Chem A 4:1586–1590
261. Li P, Hussain F, Cui P, Li Z, Yang J (2019) Boosting ionic conductivity in antiperovskite Li_3OCl via defect engineering: interstitial versus vacancy. Phys Rev Materials 3:115402
262. Yin L, Yuan H, Kong L, Lu Z, Zhao Y (2020) Engineering Frenkel defects of anti-perovskite solid-state electrolytes and their applications in all-solid-state lithium-ion batteries. Chem Commun 56:1251–1254
263. Dawson JA, Canepa P, Famprikis T, Masquelier C, Islam MS (2018) Atomic-scale influence of grain boundaries on Li-ion conduction in solid electrolytes for all-solid-state batteries. J Am Chem Soc 140:362–368

264. Lü X, Howard JW, Chen A, Zhu J, Li S, Wu G, Dowden P, Xu H, Zhao Y, Jia Q (2016) Antiperovskite Li_3OCl superionic conductor films for solid-state Li-ion batteries. Advanced Science 3:1500359
265. Chen B, Xu C, Zhou J (2018) Insights into grain boundary in lithium-rich anti-perovskite as solid electrolytes. J of the Electrochem Society 165:A3946–A3951
266. Wang Z, Xu H, Xuan M, Shao G (2018) From anti-perovskite to double anti-perovskite: tuning lattice chemistry to achieve superfast Li^+ transport in cubic solid lithium halogen–chalcogenides. J Mater Chem A 6:73–83
267. Xu H, Xuan M, Xiao W, Shen Y, Li Z, Wang Z, Hu J, Shao G (2019) Lithium ion conductivity in double antiperovskite $Li_{6.5}OS_{1.5}I_{1.5}$: alloying and boundary effects. ACS Appl Energy Mater 2:6288–6294
268. Lai Z, Feng W, Dong X, Zhou X, Wang Y, Xia Y (2021) Lithium dendrites suppressed by low temperature in-situ anti-perovskite coated garnet solid-state electrolyte. J of Power Sources 500:229982
269. Sugumar MK, Yamamoto T, Motoyama M, Iriyama Y (2020) Room temperature synthesis of anti-perovskite structured Li_2OHBr. Solid State Ionics 349:115298
270. Lü X, Wu G, Howard JW, Chen A, Zhao Y, Daemen LL, Ji Q (2014) Li-rich anti-perovskite Li_3OCl films with enhanced ionic conductivity. Chem Commun 50:11520–11522
271. Rajagopal R, Park M-H, Subramanian Y, Jung YJ, Ryu K-S (2021) Synthesis and electrochemical performance of antiperovskite-like Li_3SI solid electrolyte. J Electroanal Chem 895:115477
272. Wu MS, Xu B, Luo WW, Sun BZ, Ouyang CY (2020) Interfacial properties and Li-ion dynamics between Li_3OCl solid electrolyte and Li metal anode for all solid state Li metal batteries from first principles study. Electrochim Acta 334:135622
273. Yoshikawa K, Yamamoto T, Sugumar MK, Motoyama M, Iriyama Y (2021) Room temperature operation and high cycle stability of an all-solid-state lithium battery fabricated by cold pressing using soft Li_2OHBr solid electrolyte. Energy Fuels 35:12581–12587
274. Serejo JAS, Pereira JS, Mouta R, Rego LGC (2021) Sluggish anion transport provides good kinetic stability to the anhydrous anti-perovskite solid electrolyte Li_3OCl. Phys Chem Chem Phys 23:6964–6973
275. Rajagopal R, Subramanian Y, Hwang G, Jung YJ, Ryu KS (2022) Improved ionic conductivity and structural transition from (nLi2S-LiI)-(P2S5) solid solutions to LixP2SyI crystalline electrolytes. J Alloys and Comp 900:163435
276. Hong HY-P (1978) Crystal structure and ionic conductivity of $Li_{14}Zn(GeO_4)_4$ and other new Li^+ superionic conductors. Mater Res Bull 13:117–124
277. Alpen UV, Bell MF, Wichelhaus W (1978) Ionic conductivity of $Li_{14}Zn(GeO_4)_4$ (LISICON). Electrochim Acta 23:1395–1397
278. Du YA, Holzwarth NAW (2007) Li ion diffusion mechanisms in the crystalline electrolyte γ-Li_3PO_4. J Electrochem Soc 154:A999–A1004
279. Sun Y-Q, Luo X-T, Zhu Y-S, Liao X-J, Li C-J (2022) Li_3PO_4 electrolyte of high conductivity for all-solid-state lithium battery prepared by plasma spray. J Eur Ceram Soc 42:4239–4247
280. Rodger AR, Kuwano J, West AR (1985) Li^+ ion conducting γ solid solutions in the systems Li_4XO_4-Li_3YO_4: X=Si, Ge, Ti; Y=P, As, V; Li_4XO_4-$LiZO_2$: Z=Al, Ga, Cr and Li_4GeO_4-Li_2CaGeO_4. Solid State Ionics 15:185–198
281. Burmakin EI, Voronin VI, Shekhtman GS (2003) Crystalline structure and electroconductivity of solid electrolytes $Li_{3.75}Ge_{0.75}V_{0.25}O_4$ and $Li_{3.7}Ge_{0.85}W_{0.15}O_4$. Russ J Electrochem 39:1124–1129
282. Deng Y, Eames C, Fleutot B, David R, Chotard JN, Suard E, Masquelier C, Islam MS (2017) Enhancing the Lithium ion conductivity in lithium superionic conductor (LISICON) solid electrolytes through a mixed polyanion effect. ACS Appl Mater Interfaces 9:7050–7058
283. Zhao G, Suzuki K, Okumura T, Takeuchi T, Hirayama M, Kanno R (2022) Extending the frontiers of lithium-ion conducting oxides: development of multicomponent materials with γ-Li_3PO_4-type structures. Chem Mater 34:3948–3959
284. Bruce PG, West AR (1983) The A-C conductivity of polycrystalline LISICON, $Li_{2+2x}Zn_{1-x}GeO_4$, and a model for intergranular constriction resistances. J Electrochem Soc 130:662–669
285. Okumura T, Taminato S, Takeuchi T, Kobayashi H (2018) Minimizing the grain boundary resistance of Li-ion-conducting oxide electrolyte by controlling liquid-phase formation during sintering. ACS Appl Energy Mater 1:6303–6311
286. Robertson AD, West AR, Ritchie AG (1997) Review of crystalline lithium-ion conductors suitable for high temperature battery applications. Solid State Ionics 104:1–11
287. Okumura T, Takeuchi T, Kobayashi H (2021) All-solid-state batteries with $LiCoO_2$-type electrodes: realization of an impurity-free interface by utilizing a cosinterable $Li_{3.5}Ge_{0.5}V_{0.5}O_4$ electrolyte. ACS Appl Energy Mater 4:30–34
288. Okumura T, Taminato S, Miyazaki Y, Kitamura M, Saito T, Takeuchi T, Kobayashi H (2020) LISICON-based amorphous oxide for bulk-type all-solid-state lithium-ion battery. ACS Appl Energy Mater 3:3220–3229
289. Nagata H, Akimoto J (2021) All-oxide solid-state lithium-ion battery employing $50Li_2SO_4$–$50Li_2CO_3$ glass electrolyte. J Power Sources 491:229620
290. Kato T, Yoshida R, Yamamoto K, Hirayama T, Motoyama M, West WC, Iriyama Y (2016) Effects of sintering temperature on interfacial structure and interfacial resistance for all-solid-state rechargeable lithium batteries. J of Power Sources 325:584–590
291. Nagata H, Akimoto J (2019) Improvement of inter-particle contact in positive electrodes using the composite deformable solid electrolyte in an oxide-type all-solid-state Lithium ion battery. Chem Lett 48:891–893
292. Nagata H, Akimoto J (2021) Excellent deformable oxide glass electrolytes and oxide-type all-solid-state Li_2S–Si batteries employing these electrolytes. ACS Appl Mater Interfaces 13:35785–35794
293. Souquet JL (1981) Ionic transport in amorphous solid electrolytes. Annu Rev Mater Sci 11:211–231
294. Bates JB, Dudney NJ, Gruzalski GR, Zuhr RA, Choudhury A, Luck CF, Robertson JD (1993) Fabrication and characterization of amorphous lithium electrolyte thin films and rechargeable thin-film batteries. J Power Sources 43(1–3):103–110
295. Reddy MV, Julien CM, Mauger A, Zaghib K (2020) Sulfide and oxide inorganic solid electrolytes for all-solid-state Li batteries: a review. Nanomaterials 10:1606
296. Kulkarni AR, Maiti HS, Paul A (1984) Fast ion conducting lithium glasses. Bull Mater Sci 6:201–221
297. Meikhall MS, Gohar IA, Megahed AA (1993) Lithium borosilicate glasses as electrolyte for solid state batteries. J Phys D Appl Phys 26:1125–1129
298. Kang ET, Kim MJ, Kim JD (2007) Relationship between ionic conductivity and composition of Li_2O-ZrO_2-SiO_2 glasses determined from mixture design. J Korean Ceram Soc 44:219–223
299. Xia H, Wang HL, Xiao W, Lai MO, Lu L (2009) Thin film Li electrolytes for all-solid-state micro-batteries. Int J Surf Sci Eng 3:23–43
300. Nagao K, Shigeno M, Inoue A, Deguchi M, Kowada H, Hotehama C, Sakuda A, Tatsumisago M, Hayashi A (2022) Lithium-ion conductivity and crystallization temperature of multicomponent oxide glass electrolytes. Journal of Non-Crystalline Solids: X 14:100089
301. Sasaki S, Ono A, Suzuki A, Takei M, Suzuki K, Hirayama M, Kanno R (2022) Combinatorial synthesis and ionic conductivity of

amorphous oxynitrides in a pseudo-ternary Li_3PO_4-Li_4SiO_4-$LiAlO_2$ system. Electrochemistry 90:037008
302. Tron A, Nosenko A, Park YD, Mun J (2017) Synthesis of the solid electrolyte Li_2O–LiF–P_2O_5 and its application for lithium-ion batteries. Solid State Ionics 308:40–45
303. Tron A, Nosenko A, Park YD, Mun J (2019) The solid electrolytes Li_2O–LiF–Li_2WO_4–B_2O_3 with enhanced ionic conductivity for lithium-ion battery. J Ind Eng Chem 73:62–66
304. Adhwaryu VA, Kanchan DK (2022) Effect of lithium iodide on transport phenomenon in lithium borophosphate glass electrolyte. J Non-Cryst Solids 583:121474
305. Kaup K, Bazak JD, Vajargah SH, Wu X, Kulisch J, Goward GR, Nazar LF (2020) A Lithium oxythioborosilicate solid electrolyte glass with superionic conductivity. Adv Energy Mater 10:1902783
306. Lacivita V, Artrith N, Ceder G (2018) Structural and compositional factors that control the Li-Ion conductivity in LiPON electrolytes. Chem Mater 30:7077–7090
307. Lee S, Jung S, Yang S, Lee J-H, Shin H, Kim J, Park S (2022) Revisiting the LiPON/Li thin film as a bifunctional interlayer for NASICON solid electrolyte-based lithium metal batteries. Appl Surf Sci 586:152790
308. Ko J, Yoon YS (2022) Lithium phosphorus oxynitride thin films for rechargeable lithium batteries: applications from thin-film batteries as micro batteries to surface modification for large-scale batteries. Ceram Int 48:10372–10390
309. Fleutot B, Pecquenard B, Martinez H, Levasseur A (2012) Thorough study of the local structure of LiPON thin films to better understand the influence of a solder-reflow type thermal treatment on their performances. Solid State Ionics 206:72–77
310. Ko J, Yoon YS (2020) Influence of process conditions on structural and electrochemical properties of lithium phosphorus oxynitride thin films. Ceram Int 46:20623–20632
311. Le Van L, -Jodin, A. Claudel, C. Secouard, F. Sabary, J.-P. Barnes, S. Martin, (2018) Role of the chemical composition and structure on the electrical properties of a solid state electrolyte: case of a highly conductive LiPON. Electrochim Acta 259:742–751
312. Lacivita V, Westover AS, Kercher A, Phillip ND, Yang G, G. Veith … and N.J. Dudney, (2018) Resolving the amorphous structure of lithium phosphorus oxynitride (Lipon). J Am Chem Soc 140(35):11029–11038
313. Famprikis T, Galipaud J, Clemens O, Pecquenard B, Le Cras F (2019) Composition dependence of ionic conductivity in LiSiPO(N) thin-film electrolytes for solid-state batteries. ACS Appl Energy Mater 2:4782–4791
314. Wu S, Xiao R, Li H, Chen L (2022) Ionic conductivity of LiSiON and the effect of amorphization/heterovalent doping on Li^+ diffusion. Inorganics 10:45
315. Na D, Lee B, Yoon B, Seo I (2020) A solid-state thin-film electrolyte, lithium silicon oxynitride, deposited by using RF sputtering for thin-film batteries. J Korean Phys Soc 76:855–859
316. Wu T, Dai W, Ke M, Huang Q, Lu L (2021) All-solid-state thin film μ-batteries for microelectronics. Advanced Science 8:2100774
317. Ziebert C, Knorr A, Thiel N, Fischer J, Kohler R, Pröll J, Pfleging W, Ulrich S, Seifert HJ (2011) Combinatorial approach for the development of solid state electrolytes in the system Li-V-Si-O for thin film Li-ion batteries. LiBD-5– Electrode materials - Arcachon, France 12–17 June : O45
318. Yada C, Iriyama Y, Abe T, Kikuchi K, Ogumi Z (2006) Amorphous Li–V–Si–O thin films as high-voltage negative electrode materials for thin-film rechargeable lithium-ion batteries. J of the Electrochem Society 153:A1148–A1153
319. Jetybayeva A, Uzakbaiuly B, Mukanova A, Myung S-T, Bakenov Z (2021) Recent advancements in solid electrolytes integrated into all-solid-state 2D and 3D lithium-ion microbatteries. J Mater Chem A 9:15140–15178
320. Salot R, Martin S, Oukassi S, Bedjaoui M, Ubrig J (2009) Microbattery technology overview and associated multilayer encapsulation process. Appl Surf Sci 256 Supplement:S54-S57
321. Westover AS, Dudney NJ, Sacci RL, Kalnaus S (2019) Deposition and confinement of Li metal along an artificial Lipon-Lipon interface. ACS Energy Lett 4:651–655
322. Cao D, Sun X, Li Q, Natan A, Xiang P, Zhu H (2020) Lithium dendrite in all-solid-state batteries: growth mechanisms, suppression strategies, and characterizations. Matter 3:57–94
323. Du M, Liao K, Lu Q, Shao Z (2019) Recent advances in the interface engineering of solid-state Li-ion batteries with artificial buffer layers: challenges, materials, construction, and characterization. Energy Environ Sci 12:1780–1804
324. Song J, Jacke S, Becker D, Hausbrand R, Jaegermann W (2011) Stabilization of thin film $LiCoO_2$ electrode by LiPON coating. Electrochemical and Solid State Letters 14:A11–A13
325. Kim Y, Veith GM, Nanda J, Unocic RR, Chi M, Dudney NJ (2011) High voltage stability of $LiCoO_2$ particles with a nanoscale Lipon coating. Electrochim Acta 56:6573–6580
326. Martha SK, Nanda J, Kim Y, Unocic RR, Pannala S, Dudney NJ (2013) Solid electrolyte coated high voltage layered–layered lithium-rich composite cathode: $Li_{1.2}Mn_{0.525}Ni_{0.175}Co_{0.1}O_2$. J Mater Chem A 1:5587–5595
327. Yang S-Y, Shadike Z, Wang W-W, Yue X-Y, Xia H-Y, Bak S-M, Du Y-H, Li H, Fu Z-W (2022) An ultrathin solid-state electrolyte film coated on $LiNi_{0.8}Co_{0.1}Mn_{0.1}O_2$ electrode surface for enhanced performance of lithium-ion batteries. Energy Storage Materials 45:1165–1174
328. Yu T, Yang X, Yang R, Bai X, Xu G, Zhao S, Duan Y, Wu Y, Wang J (2021) Progress and perspectives on typical inorganic solid-state electrolytes. J Alloy Compd 885:161013